Distinct networks of periaqueductal gray columns in pain and threat processing

Wang, Sean; Veinot, Jennika; Goyal, Amita; Khatibi, Ali; Lazar, Sara; Ali Hashmi, Javeria

DOI:
10.1016/j.neuroimage.2022.118936

NeuroImage 250 (2022) 118936

Contents lists available at ScienceDirect

NeuroImage

journal homepage: www.elsevier.com/locate/neuroimage

Distinct networks of periaqueductal gray columns in pain and threat processing

Sean Wang[a], Jennika Veinot[a], Amita Goyal[a], Ali Khatibi[b], Sara W. Lazar[c], Javeria Ali Hashmi[c,*]

[a] Department of Anesthesia, Pain Management & Perioperative Medicine, Dalhousie University, NSHA, Halifax, Canada, B3H 1V7
[b] Centre of Precision Rehabilitation for Spinal Pain, School of Sport, Exercise and Rehabilitation Sciences, College of Life and Environmental Sciences, University of Birmingham, Edgbaston, B15 2TT, United Kingdom
[c] Harvard Medical School, Mass General Hospital, Boston, MA, US 02129

ARTICLE INFO

Keywords:
brainstem
PAG
threat
pain
expectation
networks
descending inhibition
top-down
prediction
salience
sympathetic
parasympathetic
nociception
functional connectivity
time varying
resting state
task based connectivity
functional MRI
fMRI

ABSTRACT

Noxious events that can cause physical damage to the body are perceived as threats. In the brainstem, the periaqueductal gray (PAG) ensures survival by generating an appropriate response to these threats. Hence, the experience of pain is coupled with threat signaling and interfaces in the dl/l and vlPAG columns. In this study, we triangulate the functional circuits of the dl/l and vlPAG by using static and time-varying functional connectivity (FC) in multiple fMRI scans in healthy participants (n = 37, 21 female). The dl/l and vlPAG were activated during cue, heat, and rating periods when the cue signaled a high threat of experiencing heat pain and when the incoming intensity of heat pain was unknown. Responses were significantly lower after low threat cues. The two regions responded similarly to the cued conditions but showed prominent distinctions in the extent of FC with other brain regions. Thus, both static and time-varying FC showed significant differences in the functional circuits of dl/l and vlPAG in rest and task scans. The dl/lPAG consistently synchronized with the salience network and the thalamus, suggesting a role in threat detection, while the vlPAG exhibited more widespread synchronization and frequently connected with memory/language and sensory regions. Hence, these two PAG regions process heat pain when stronger pain is expected or when it is uncertain, and preferentially synchronize with distinct brain circuits in a reproducible manner. The dl/lPAG seems more directly involved in salience detection, while the vlPAG seems engaged in contextualizing threats.

1. Introduction

Pain can be experienced even before a noxious event causes harm, and the experience of pain is necessary for predicting the resulting tissue damage. Pain intensity conveys information about the threat level perceived from a noxious event. However, this process is bi-directional; the bottom-up nociceptive input is processed and modulated by top-down factors such as cues, inferred context and prior mental states (Bouton and Bolles, 1979; Fadok et al., 2017; LeDoux and Daw, 2018).

Top-down factors modulate nociceptive input and alter the experience of pain through a connected network of cortical and brainstem regions (Lin et al., 2014; Fields, 2018). Of specific importance in the brainstem are the periaqueductal gray (PAG) and rostral ventromedial medulla (RVM) (Basbaum and Fields, 1984; Lumb, 2004). Projections from this system descend to the spinal cord to alter spinal dorsal horn not been thoroughly tested for reproducibility (Harrison et al., 2010; Radua et al., 2014; George et al., 2019).

The PAG is organized in four columnar subdivisions of which the dorsolateral/lateral (dl/lPAG) and ventrolateral (vlPAG) regulate responses to nociceptive inputs (Carrive, 1993). This columnar organization has been recorded in a few animal studies (Lumb et al., 2002; Keay and Bandler, 2002) and was more recently demonstrated with brain imaging in humans (Ezra et al., 2015; Coulombe et al., 2016). The dl/lPAG is functionally organized for generating responses that require a sympathetic motor fight, flight, and fright response (Kincheski et al., 2012; Mochny et al., 2013; Watson et al., 2016). It receives inputs from nociceptors that have high conduction velocities (A-delta fibers), producing sharp pain sensations with shorter attention latencies (Bandler et al., 2000; Parry et al., 2008; Koutsikou et al., 2017) and is linked with rapid and active responses to physical threats (Roelofs, 2017). The vlPAG re-

* **Corresponding author at:** 5820 University Avenue, Dickson, 4th Floor, room 4207, Department of Anesthesia, Pain Management & Perioperative Medicine, Dalhousie University, NSHA, Halifax, Canada, B3H 1V7.
E-mail address: javeria.hashmi@dal.ca (J.A. Hashmi).

https://doi.org/10.1016/j.neuroimage.2022.118936.
Received 9 April 2021; Received in revised form 2 December 2021; Accepted 24 January 2022
Available online 29 January 2022.

ceives nociceptive input from, among others, the slow conduction polymodal C-fibers (Benarroch, 2012; Lumb et al., 2002; Satpute et al., 2013; Tovote et al., 2016) that modulate parasympathetic responses, and is involved in freezing behavior in response to threats (Faull et al., 2016). As such, it is implicated in passive emotional coping strategies such as quiescence, vasodepression, and freeze and appease responses (Keay et al., 1997; Carrive et al., 1997). The respective roles of these two regions in processing threat and pain are deduced from animal studies and has not been thoroughly studied in the human brain.

Here, we study activation and functional connectivity in three task-related and one resting state MR scan from a dataset designed for investigations of cued pain response in healthy subjects. During the task, visual cues suggested the incoming stimulus intensity, referred to here as cued threat. Participants observed the cued threat (prediction), experienced heat pain stimuli (sensory evidence), and then rated the evoked pain intensity. The effects of the cues were evaluated by comparing pain ratings after presenting cues that signaled high or low cued threat, or when the strength of incoming stimulus was unknown. We used a data-driven technique (Hashmi et al., 2013) for measuring PAG responses to the three selected conditions. Next, we tested the brain-wide circuits that dl/l and vlPAG participated in. Towards this goal, we first looked at the synchronizations between dl/l and vlPAG with other brain regions during the epochs in which high, low, and unknown pain threats were presented visually before the heat stimuli at the same intensity. Second, we compared whole brain dl/l and vlPAG functional connectivity for the entire resting state and task scans. Third, we used time varying functional connectivity (TVFC) to instantiate whether the dl/lPAG and vlPAG behave synchronously with other brain regions from moment to moment when observed under the same experimental conditions. Using the TVFC method, we identified differences in regions connecting preferentially with dl/lPAG and vlPAG on a moment to moment basis. We also assessed if these regions differ in the total number of nodes that they connect with. To gain complementary insights from static and dynamic functional connectivity analysis, we assessed the brain wide connectivity of dl/lPAG and vlPAG during rest and task scans with static and with time-varying FC. This triangulation using multiple approaches consistently demonstrated significant and whole brain corrected differences in the dl/lPAG and vlPAG connectivity patterns. The within-subject design, combined with the use of a large number of volumes from different types of scans (rest and task), diverse analytical approaches (activation, static and time-varying functional connectivity), and observations from a control brainstem ROI, were used to establish the validity of the findings.

2. Methods

Study data. This study is a component of a larger study directed at developing biopsychosocial and neurological markers associated with treatment failure in chronic back pain (clinicalTrials.gov: RCT #NCT02991625). The main goal of the larger study is to establish the scope and limitations of neuroimaging for identifying reproducible and reliable findings from brain data that can pinpoint chronic pain mechanisms. In this study, we investigate the specificity and reproducibility of properties of the PAG columnar pathways in healthy controls. The task design and whole-brain, voxel-wise activations in task-related data have previously been published (Lim et al., 2020). This study delineates the activations, task-related synchronizations, and functional connectivity characteristics of the PAG columns in a model-free, data-driven manner.

Participants. The study protocol was approved by the Nova Scotia Health Research Ethics Board. Data was collected in healthy participants (21 female; mean age ± SD of 31.23 ± 10.91 years; range of 20–56 years). From the 42 subjects who participated in the study, resting-state data was successfully collected from 39 participants and complete pain task scans were available in 38 subjects. Participants were excluded if they (1) had ongoing acute or chronic pain, were (2) taking pain medication, (3) pregnant, or (4) unfit for MRI scanning (i.e., cardiac and respiratory conditions that would lead to interference with the study, metal implants, dental braces, claustrophobia), or (5) had neurological or psychiatric disorders. Before pain task scans, all participants first underwent structural and resting-state fMRI scans. Subsequently, they underwent task scans while performing the pain expectation task described below.

Study protocol. The first set of psychophysical measurements collected were heat evoked pain threshold and heat evoked pain tolerance. Next, participants were trained in seeing visual cues across a screen, experiencing a heat stimulus, and rating the intensity of their pain on a scale in response to said heat stimuli, which were held at 45 °C and 47 °C in a random order.

Epoch design. For a summary depiction, see Fig. 1A. The visual cues presented during the task would either predict the stimulus intensity (example: “the incoming heat stimulus is at 9% intensity”) or prompt that the stimulus intensity is unknown (“the incoming heat stimulus intensity is unknown”). The visual cues lasted 4.75 s, and were followed by a delay screen of 1.9 s (black screen with white fixation cross). Heat stimuli started from a baseline temperature (35 °C), increased to plateau at a peak intensity, then decreased back down to baseline, at a rate of 4 °C/second. Each stimulus lasted 8 s. Plateau durations were dependent on the peak intensity; thus, a peak intensity of 45 °C and 47 °C would last for 3 and 2 s, respectively. After another delay screen of 4.75 s, participants rated their perceived pain experience within 6 s with the numerical rating scale (NRS). The interval between epochs was jittered at delays of 1.9s-8.55 s.

Task conditions. Pain task scans consisted of three types of epochs: matched, mismatched at level 1, and mismatched at level 2. See Fig. 1B-D for a schematic.

The first run consisted of epochs containing only the matched condition, where the cue-values correctly predicted the heat stimulus intensity. In the matched condition run, participants experienced peak stimulus temperatures (43.8–47 °C) that changed linearly with the stimulus intensity values shown in the cues. In this run, cues were shown as a range of 10 points: for instance, the cues would read that the incoming stimulus intensity is at 11–20%. Thus, each time the cue value range increased or decreased by 10 points, the stimulus temperature increased or decreased by 0.4 °C. Thus, participants were trained to predict the pain intensity from the cue values. The neuroimaging data from the matched run was collected in only 19 participants and was thus not used in the present study. This task run was designated as the training run, while subsequent runs were designated as test runs. The three test runs were administered while simultaneously collecting task fMRI scans. Hence, the three test runs are denoted in this paper as task scans 1 to 3.

In the three test runs, epochs containing prediction errors were introduced and discrete cue values were shown: for example, the cue would read that the incoming stimulus intensity is at 15%. Thus, in the first test run (also called mismatched condition level 1), cue values ranging from 0–40 were paired with a 45 °C stimulus only and cue values ranging from 60–100 were presented before 47 °C stimuli. In other epochs, the 45 °C and the 47 °C were paired with cue values identical to those in the matched run. This type of pairing produced a range of prediction errors (difference between expected and actual stimulus intensity) varying from 0–1.2 °C. All epochs were presented in a pseudorandom order.

In the remaining two test runs (labeled as mismatched condition level 2), epochs containing higher prediction errors were introduced, with low threat cues ranging from 1–30 now paired with 47 °C stimuli. The prediction errors for these epochs thus ranged from 1.3–3.2 °C. In order to prevent extinction effects, epochs containing the lower prediction errors of 0–1.2 °C as in the mismatch level 1 were also used. Hence, cues ranging from 1–40 were paired with a 45 °C stimulus. Similarly, cues ranging from 60–100 were presented with 47 °C stimuli. This approach of combining epochs produced prediction errors at a range of 0–3.2 °C, with which we could measure pain responses for cue val-

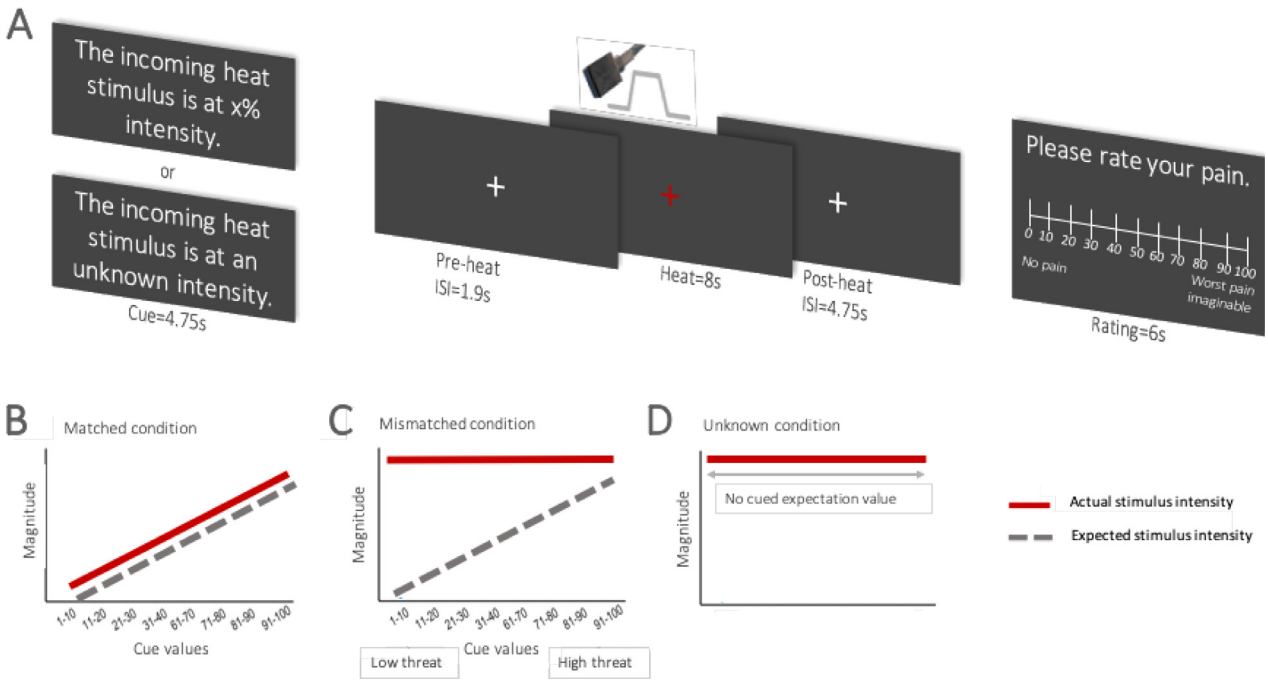

Fig. 1. A schematic depiction of the experimental methods and conditions. [A] Participants were first prompted with threat cues (1–100) that either displayed estimates of the incoming stimulus intensities (top left) or the stimulus intensities were said to be unknown (bottom left). The noxious heat stimuli were then delivered to the participants. Subsequently, participants were prompted to give pain ratings ranging from 0–100. There were three conditions that arose from this experimental paradigm. [B] Matched condition. The threat cue matched incoming stimulus intensity. [C] Mismatched condition. The threat cues increased linearly while the stimulus intensity stayed constant at 47 ˚C. Low threat cues include 1–20. High threat cues include 91–100. [D] Unknown threat condition. The threat cue did not give an intensity value (see 1A, bottom left). The threat intensity was held constant at 47 ˚C. Therefore, there were no cued threats.

ues ranging from 0–100 paired with the exact same stimulus intensity of 47 ˚C. Using these epochs, and by sorting them in ascending order based on cue-values, we have previously reported that, although the stimulus intensity remained the same, the pain responses linearly increased with the cue values, suggesting a strong impact of top-down cues on pain. There was a marked difference in pain ratings where response to stimuli paired with low threat cues (1–30) was attenuated relative to the response to those paired with high threat cues for the same stimulus temperature of 47 ˚C (Lim et al., 2020). The large effect size of this difference allowed us to investigate the brain systems that alter pain intensity with changes in the expectation of pain threats. In this study, we used the responses on the extreme ends for our analyses, by selecting epochs paired with the 47 ˚C stimuli containing the highest threat cues (range 90–100) and the lowest threat cues (range 1–20).

In addition, we used epochs in which the cues signaled that “the incoming heat stimulus intensity is unknown”, that were interspersed between the cued condition. These epochs were presented with either 45 ˚C or 47 ˚C stimuli. In this study, the ‘unknown’ cues paired with 47 ˚C stimuli were used in the analysis. Responses from 4–6 repetitions for each type of epoch (high threat: HT, low threat: LT) and unknown threat (unknown) were averaged.

3. *Functional MRI scans and preprocessing*

Functional MRI scans were collected using a 3T MRI scanner (Discovery MR750; General Electric Medical Systems, Waukesha, WI, USA) with a 32-channel head coil (MR Instruments, Inc.; Minneapolis, MN, USA) at the Halifax Infirmary Site, QEII Health Sciences Centre, Halifax, NS, Canada. To support patient comfort and minimize motion, participants’ heads were fitted with foam padding, ear plugs were used to minimize the sound levels, and reminders were given before each scan to keep their head still. The following protocol was used for T1-weighted brain images (GE sequence 3D IR-FSPGR): field of view=224 × 224 mm; in-plane resolution=1 mm × 1 mm; slice thickness=1.0 mm; TR/TE=4.4/1.908 milliseconds; flip angle=9˚. The fMRI BOLD (blood oxygenation level dependent) sequence protocol used a multi-band EPI sequence: field of view=216 × 216 mm; in-plane resolution=3 mm × 3 mm; slice thickness=3.0 mm; TR/TE=950/30 milliseconds, SENSE factor of 2, acceleration factor of 3. The number of total volumes was: 500 for resting state scans, 814 for the training scan and 624 for the three pain task scans. Reverse phase encoded images were also acquired for the application of FSL’s topup for distortion correction.

All functional datasets were corrected for field map-based distortion. Data was preprocessed with AFNI (http://afni.nimh.nih.gov/afni) and FSL (http://www.fmrib.ox.ac.uk/fsl) with the scripts provided by 1000 Functional Connectomes Project (http://www.nitrc.org/projects/fcon_1000). All of the following steps for preprocessing were adapted from the parent study (Lim et al., 2020). Preprocessing carried out by AFNI included: (1) discarding the first five EPI volumes to allow for signal equilibration, (2) rigid-body motion correction of time series by aligning each volume to the mean image using Fourier interpolation, (3) skull stripping, and (4) getting an eighth image for use in registration. Preprocessing using FSL consisted of: (5) spatial smoothing using a Gaussian kernel of full-width half-maximum=6 mm, (6) grand-mean scaling of the voxel value, (7) temporal filtering (0.005–0.3 Hz) and smoothing, (8) removing linear and quadratic trends, and (9) removing of nine nuisance signals (global mean, cerebrospinal fluid, white matter, six motion parameters describing rotational and translational movement of the head) by regression in native functional space. Note that since we studied functional connectivity in both resting state and task scans, both types of scans were preprocessed using the same procedures. Due to the small size of the ROIs, we ran the activation analysis with and without spatial smoothing (Fig. 3) and did not see any significant effects of smoothing on the activation results.

The six motion parameters mentioned above were generated using FSL motion correction in native functional space. The two nuisance time courses were calculated using masks obtained from the image segmentation of the participant's T1w data and applying a tissue-type probability threshold of 80%. Registration of functional images to the MNI152 standard template was carried out using FLIRT in three steps: (1) registration of the native-space structural image to the MNI152 2 mm template using a twelve df (degrees of freedom) linear affine transformation; (2) registration of the native-space functional image to the high-resolution structural image with a six df linear transformation; (3) computation of native-functional to standard-structural warps by concatenating the matrices computed in steps (1) and (2).

For data quality verification, maximum framewise displacement (FD) and DVARS (difference of volume N to $N + 1$), were calculated to assess and exclude participants with high motion. For image quality criteria, participant data with maximum FD above 3 mm or DVARS outliers detected in more than 10% of the acquired data was used as a cut off. Any participants with values above the cut off were removed from the analysis (Saghayi et al., 2020). No participants were excluded, as the highest maximum FD obtained and highest percentage of outliers in data detected in resting state scans for all participants were 1.73 mm and 8%, respectively. For further verification, maximum FD was used as nuisance covariate in the statistical model looking at task evoked responses.

Time series extraction from parcellations. Time series were extracted from the following regions of interest (ROIs):

Whole brain parcellation. For defining ROIs, we used a previously reported parcellation scheme optimized for pain studies (Optimized Harvard-Oxford parcellation; (Hashmi et al., 2014; Hashmi et al., 2017) consisting of 130 bilateral brain regions and the brainstem). This procedure was done using a BASH script and with functions from FSL libraries. The BOLD time series were extracted from each voxel within each parcel and averaged, resulting in 130 time-series for each participant. Next, the same procedure was performed for extracting time series from the PAG regions described below and from the entire brainstem region as given in the Harvard-Oxford parcellation.

PAG seed parcellation. The parcellation procedure used a two-fold approach. First, focal PAG seed coordinates were based on previously published studies (Coulombe et al., 2016; Linnman et al., 2012). The primary coordinates of dl/l and vlPAG seeds were $x=\pm4$, $y=-31$, $z=-8$ and $x=\pm3$, $y=-32$, $z=-12$, respectively. Masks of the PAG seeds were created with the following conditions: (1) 3D voxel, (2) selection size=1, (3) search radius=1 (Woolrich et al., 2009), (4) Montreal Neurological Institute (MNI) $2mm^3$ standard space. Second, seed placements were optimized by overlapping them with an atlas previously created by (Ezra et al., 2015), based on voxel-wise diffusion MRI and probabilistic tractography. Fig. 2 shows sagittal (A, D) and axial cuts (B, C, E, F) of the different PAG seeds overlaid on each other. Data were initially analyzed separately for left and right PAG columns, however due to a lack of significant laterality, signals from the right and left masks were averaged for both the dl/l (20 voxels, 320 mm square area) and vlPAG (24 voxels, 384 mm square area).

Task evoked responses from dl/lPAG and vlPAG. In order to investigate if the dl/l and vlPAG modulate pain with changes in threat level, the portion of the time series spanning the cues, heat stimuli, and rating events were extracted. A response delay of 6 TRs was added to account for the hemodynamic response delay (Liao et al., 2002); the appropriateness of using this delay for PAG response was ascertained by visualizing the activations. Within each epoch, the mean activations for each of the three types of events were measured and compared between the three main task conditions (high threat, low threat, unknown threat). The unknown threat was used as a comparator in this analysis to test if the PAG responds only to explicitly presented cued threats or if it also responds to uncertainty when pain is expected but the intensity is unknown. Responses to cue, heat, and rating were tested between all three variables and for the dl/lPAG and vlPAG using a within-subject three-way repeated measures ANOVA with post hoc paired t-tests in SPSS (v24; IBM; Armonk, NY, USA). Note that, because right and left dl/lPAG and vlPAG responses did not show significant differences, responses from the two sides for each column were averaged for analysis. This and all subsequent analyses were conducted in the MATLAB software (R2018b; The Mathworks; Natick, MA, USA).

Control brainstem ROI, tests for artifacts and limitations. A mask covering the entire brainstem was used as a control ROI to confirm that task-related activations were not due to physiological artifacts. Thus, time series were extracted from the entire brainstem (as given in the Harvard-Oxford atlas) that covers all areas starting from the medulla and extending rostrally up to the midbrain.

To test for artifacts, we used three tests: (1) to test for global effects of physiological signals on brainstem responses, signal from the control brainstem ROI was separately analyzed to check for differences in activation between the high, low, and unknown threats, (2) maximum framewise displacement calculated from each subject was added as a covariate of no interest to the main analyses, (3) activations during cue, heat, rating in dl/lPAG and vlPAG were correlated with maximum framewise displacement using Spearman's R.

Better acquisition parameters such as a higher spatial resolution, at a higher field strength, a higher sampling rate and/or a specific field of view adapted to look at brainstem responses would be helpful for assessing the role of artifacts in mediating the findings. Keeping these limitations in view, we relied on the within-subject, group-level design and extensive triangulation. We used different scan-types (rest and task) in 2542 multibanded volumes, and different analytical approaches (data driven task response mapping, static and dynamic functional connectivity and graph metrics) to build confidence in the main findings.

Functional connectivity analysis. Because the regions of interest were small and located in the brainstem, we used functional connectivity analyses that relied on different assumptions (resting state, task-related, static, time-varying functional connectivity) to validate the results and to assess the reproducibility of the main findings.

A. Task-related synchrony within different types of epochs. To assess the BOLD response synchrony between the PAG ROIs and other parts of the brain, the time series from the whole brain parcellation, the PAG ROIs and brainstem ROI were extracted and separated for the epochs in which high, low, and unknown threat cues were paired with 47 °C stimuli (as described for the task evoked responses). The time series was divided into 40 time points windows, where each window encompassed events such as cue heat rating. This procedure was repeated for the three epochs of interest (high threat, low threat and unknown threat). These time courses were averaged for each epoch condition and each brain ROI (130 total), then correlated with the dl/lPAG and the vlPAG time courses using a zero-lag pairwise Pearson correlation. The resulting correlation matrices were statistically compared between the high-threat and low-threat epoch conditions, and between dl/lPAG and vlPAG, using a two-way repeated measures ANOVA test with a post hoc paired *t*-test. The unknown threat epoch conditions were tested post hoc as a control condition. The results were corrected with False Discovery Rate (FDR) at a q-value of 0.05.

Note that the discrete time-windows containing time points were statistically compared for each epoch type (high, low and unknown threat). To avoid redundancy, this comparison was not repeated for time varying functional connectivity analysis detailed below. In addition, each epoch time window encapsulated the events related to cue, heat and rating presentation. Because these events were of short duration (<15TRs), the FC estimated from the entire epoch captures the effects of epoch condition (high threat, low threat and unknown threat) and does not capture the specific effects of each event.

B. Static functional connectivity analysis. The dl/l and vlPAG time series were correlated with the 130 regions to define 2×130 adjacency matrices for each scan using a zero-lag pairwise Pearson correlation (Gibbons, 1985). The correlation matrices were created from the entire time series for the resting state scan. In addition, the three cor-

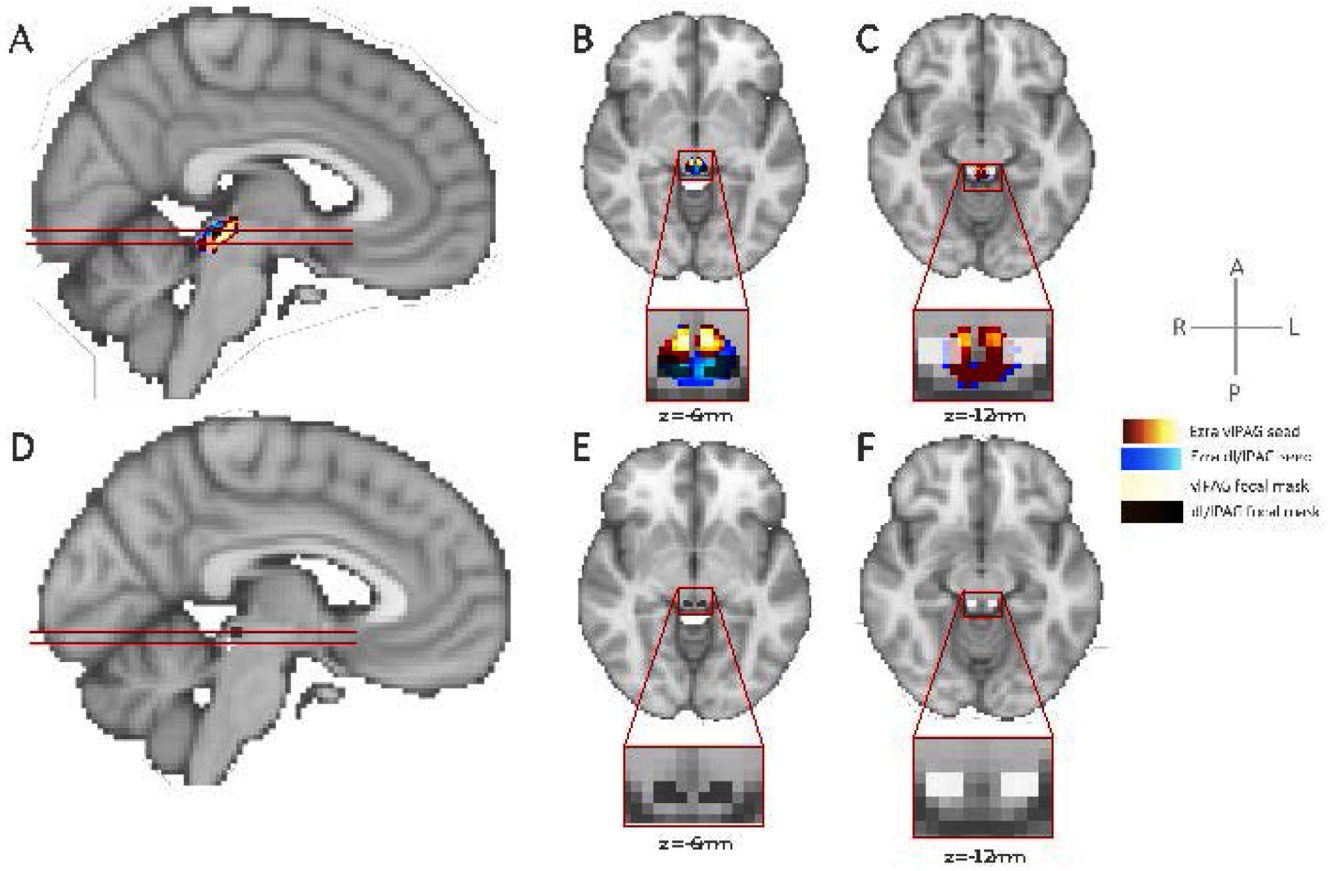

Fig. 2. Localization of the dl/l and vlPAG in MNI 2mm^3 standard space. [A] Sagittal plane slice of parcellated PAG seeds. Activations in blue-light-blue and red-yellow seeds are derived from dl/l and vlPAG, respectively. Seeds were created from the atlas made by (Ezra et al., 2015). White and black focal masks are based on previous literature (Coulombe et al., 2016; Linnman et al., 2012) and optimized by the aforementioned atlas. All focal PAG masks were created bilaterally (left and right together). [B] Axial view of the dl/lPAG focal and atlas masks. The primary coordinates of the dl/lPAG focal mask (black) were $x=\pm4$, $y=-31$, $z=-8$. [C] Axial view of the vlPAG focal and atlas masks. The primary coordinates of the vlPAG focal mask (white) were $x=\pm3$, $y=-32$, $z=-12$. [D] Sagittal plane slice of parcellated PAG seeds. White and black focal masks are shown singularly. [E] Axial view of the dl/lPAG focal mask. [F] Axial view of the vlPAG focal mask. dl/l, dorsolateral/lateral; vl, ventrolateral; PAG, periaqueductal gray; Montreal Neurological Institute; MNI. (For interpretation of the references to color in this figure legend, the reader is referred to the web version of this article.)

relation matrices generated from the time series for each of the three task scans were averaged to measure mean task-related static functional connectivity. The dl/l and vlPAG functional connectivity were compared by using a paired *t*-test for the resting state scans and for the average connectivity matrices from the three task scans. Significance was set at $p<0.05$ and corrected for multiple comparisons with FDR at $q<0.05$.

C. Time-varying functional connectivity. Time-varying functional connectivity was computed using a sliding window approach (Calhoun et al., 2014; Qin et al., 2015) in MATLAB. Each preprocessed brain signal was div ided into temporal segments with a window size of 38 s (40TRs). The Pearson correlation coefficients were calculated for the dl/lPAG with the 130 nodes or the vlPAG with the 130 nodes for that time window (40TRs) and saved. Each time the window was advanced by one TR, 2 × 130 matrix was calculated and saved. This procedure was done for the resting state scans to yield a total of 457 matrices of 130 × 2 connections for dl/lPAG and vlPAG per subject. This procedure was repeated for each of the task scans to yield three 580 matrices of 130 × 2 ROIs. Additionally, to normalize the coefficient values of correlation matrices, we applied Fisher's z-transformation to each correlation matrix. Next, the upper triangular part of each correlation matrix was removed.

To assess the overall difference in the extent to which dl/lPAG and vlPAG engage with other parts of the brain, the FC from each window in each scan was averaged across time windows, and the mean FC was compared between dl/lPAG and vlPAG using a paired *t*-test and corrected for multiple comparisons for the number of ROIs using FDR. To illustrate the differences in the durations for which dl/l and vlPAG engage and disengage from their preferred networks, we plotted the changes in TVFC for each window for the dl/lPAG and vlPAG with a few exemplar regions separately for the three task scans.

The values for time-varying functional connectivity for the dl/l and vlPAG with other brain regions were contrasted with each other for the resting state scans using paired t-tests for each time window. The time varying FC matrices was then generated for the three task-related scans. The matrices from all time windows within a scan were averaged and the averaged matrix was contrasted between the dl/l and vlPAG with other brain regions. Next, time varying functional connectivity between dl/l and vlPAG with specific exemplar regions were plotted separately for each of the three task scans, to visualize the moment by moment changes and to explicitly demonstrate the effects observed in the averaged results.

D. Analysis of degree (total number of brain-wide connections) in static and time varying FC. The total number of brain wide connections (degree) of dl/lPAG and vlPAG were calculated using the Brain Connectivity Toolbox for MATLAB (Rubinov and Sporns, 2010). Degree was measured for each node in the static FC correlation matrix for the resting state scan and in each of the three task scan correlation matrices separately. Next, the degree of dl/lPAG was contrasted with the degree of vlPAG for each of the four scans (resting state and the task scans 1–3) using a paired *t*-test with FDR correction. The degree was averaged for

all windows within and between each scan and compared between dl/l and vlPAG.

Next, degree was estimated for the time-varying FC matrices in the resting state scan and in the three task-related scans. Thus, we could assess the changes in brain wide FC of these two regions from moment to moment. The degree values were contrasted between dl/lPAG and vlPAG for each static and time-varying FC window. In this way, we statistically identified regions of interest and the time points in which each of these regions showed higher FC. Significance was set at $p<0.05$ and corrected for multiple comparisons with False Discovery Rate (FDR).

4. Results

4.1. A. Behavioral results

A1. Cued threat levels alter pain intensity evoked by a heat stimulus. As was previously reported (Lim et al., 2020), different levels of threat presented as visual cues before heat stimuli of the same intensity had a significant impact on the pain ratings. Thus, HT cues (selected between 90–100) resulted in significantly higher pain ratings (mean=50.10 ± 25.86) relative to LT cues (mean=20.44 ± 16.30) for the same stimulus intensity of 47 ˚C stimuli. The heat stimuli that followed the cues signaling unknown stimulus intensity also produced pain ratings equivalent to those evoked by heat stimuli paired with HT cues (mean=47.84 ± 24.11).

Significant differences in pain ratings were demonstrated when HT, LT, and unknown threat conditions were compared with paired-sample t-tests. Pain ratings differed significantly between HT and LT ($t(35)=-9.118$, $p<0.001$) and between LT and unknown ($t(35)=-9.517$, $p<0.001$) threat conditions. The difference in pain ratings between HT and unknown threat conditions was found to be insignificant ($t(35)=1.607$, $p = 0.117$).

4.2. B. Task activations and synchronisations

B1. BOLD activations in task condition epochs. In order to investigate whether the dl/l and vlPAG respond to different types of cued threat, their time series during the cues, heat stimuli, and rating periods were extracted. The responses to these three events were averaged (see Methods) and compared directly between high, low, and unknown threat conditions.

Overall, both dl/l and vlPAG showed deactivation for both the HT and the unknown cue events, and then activated strongly during the heating and rating events. But when LT cues were presented, both PAG regions showed a small but attenuated activation to the cues and remained attenuated for the heating and rating events. The overall contrast between dl/lPAG and vlPAG in mean activations to the task events was not significant ($p>0.05$). A three-way repeated measures ANOVA (event type x threat level x dl/l or vlPAG activation), showed a significant interaction effect ($F^{(4, 140)}=2.822$, $p = 0.027$).

The dl/l and vlPAG mean activations observed separately for event type (cue, heat, rating) and threat levels (HT, LT, unknown) showed a few significant effects. First, for dl/lPAG (Fig. 3D), the response during the cue event was greater for LT vs. unknown threat ($t(35)=2.907$, $p = 0.006$, Fig. 3), while for the rating period, mean activations were lower in LT vs. unknown threat ($t(35)=-4.548$, $p<0.001$). In contrast, the vlPAG responses (Fig. 3E) during the heat event were significantly higher for high vs. unknown threat ($t(35)=2.352$, $p = 0.024$), while during the rating period, both high ($t(35)=3.349$, $p = 0.002$) and unknown threat ($t(35)= -2.967$, $p = 0.005$) produced significantly greater activation than low threat. Hence, the two regions showed some differences in how they responded between epoch conditions during specific events, though overall their responses were similar during the three epoch conditions. The full repeated measures ANOVA model – event type (cue, heat, and rating) x epoch type (HT, LT, and unknown threat) x region (dl/lPAG and vlPAG) – was significant ($F^{(35)}=5.172$, $P = 0.02$).

Adding the effect of head motion (quantified as maximum frame wise displacement) had no significant effect on the overall significance ($F^{(35)}=0.624$, $p = 0.63$). There were no significant correlations between activations to cue, heat, or rating with maximum frame wise displacement ($p>0.05$). As an additional control test, activations in an ROI encompassing the entire brainstem were assessed for changes in response to cue, heat, and rating in different epoch conditions (Supplementary Figure 1), with no significant difference observed ($F^{(35)}=0.432$, $p = 0.67$).

Additional analyses for investigating the role of spatial smoothing demonstrated the same statistical trends of activations in unsmoothed data as in the smoothed data. During cue presentation, the dl/l PAG showed greater activation in the low threat epochs than in the unknown threat epochs ($p = 0.049$). During heat presentation, only the vlPAG showed a trend towards greater activation during the high threat epoch than in the low threat epoch ($p = 0.085$), and during rating period, the vlPAG showed a trend towards greater activation relative to during the high threat epochs ($p = 0.082$). For comparisons with unknown threat epochs, no contrasts were significant other than a greater activation in vlPAG in the unknown threat epochs relative to the low threat epochs ($p = 0.0051$). The subject variance appeared higher in unsmoothed data (Supplementary Figure 2). The small variations in results may be due to the statistical variance added by the noise in the unsmoothed data.

B2. Task-related synchronizations. HT and LT cues resulted in different task-related synchronizations of dl/l and vlPAG with other brain regions (see Methods for details). The overall contrast (dl/lPAG vs. vLPAG, HT vs. LT) was not significant after FDR correction ($p>0.05$). The HT versus LT contrast showed a significant change in synchrony between vlPAG and several brain regions (see Table 1). In contrast, dl/lPAG changed synchrony between the two conditions for only a few regions. For post hoc analysis, the regions that significantly changed synchrony between HT vs LT condition in vlPAG or in dl/lPAG that survived FDR correction were plotted to examine the behaviors of these two regions in HT and LT conditions. As shown in Fig. 4, both dl/l and vlPAG showed a stronger positive correlation with medial and rostral anterior cingulate regions, anterior insula, and the thalamus during HT relative to LT conditions.

In contrast, several multimodal and subcortical regions such as medial prefrontal cortex (MPFC), middle temporal gyrus (MTG), and dorsolateral prefrontal cortex (dlPFC) showed a stronger negative correlation with dl/l and vlPAG during LT conditions relative to HT condition (Fig. 4 and Table 1). The polar plot (Fig. 4B) depicts a skew towards higher connectivity with salience network regions for dl/lPAG during HT and LT conditions, and one towards sensory insula and globus pallidus for vlPAG during HT conditions.

In a posthoc analyses comparing HT and unknown threat epochs, no significant difference on synchrony for either the vlPAG or the dlPAG after correction for multiple comparisons. Similarly, the changes in synchrony between unknown threat and low threat failed to survive correction for multiple comparisons, for both vlPAG and dl/lPAG. There were no significant effects observed un unknown threat condition between vlPAG and dl/lPAG in task evoked synchronizations. Thus, the main change in synchronizations between PAG regions with other brain regions occurred between the high vs the low threat condition, and the high threat and unknown threat conditions produced similar effects.

There was no significant difference in whole brain synchronization with the control brainstem signal between HT, LT, or unknown conditions after multiple comparison correction ($p>0.05$).

4.3. C. Functional connectivity analysis

Next, to identify how the dl/l and vlPAG connect with other brain regions while participating in top-down effects on pain, we observed how they differ in their functional connectivity with other brain regions during the pain task scans. Results are shown for static followed by time-varying functional connectivity analysis.

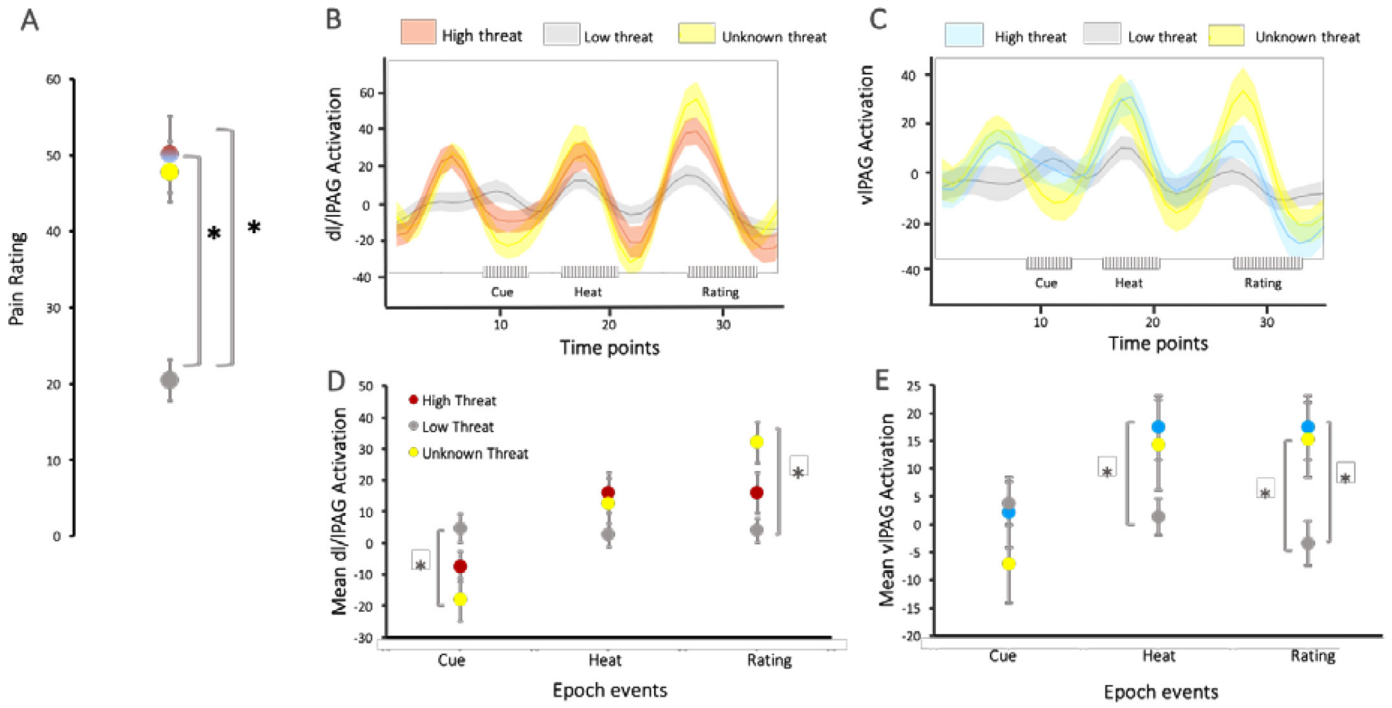

Fig. 3. Comparison of dl/l and vlPAG activations in three conditions – high threat, low threat, and unknown threat – across three chronological events: cue, heat, and rating. [A] Significant differences in pain ratings between high and low, and unknown and low, threat conditions. Significant findings ($p<0.05$) are demarcated by the asterisks (*). [B] and [C] Data-driven response patterns for dl/lPAG [B] and vlPAG [C] activations showing high threat (red), low threat (gray), and unknown (yellow) conditions. [D] and [E] Activation to events averaged for the cue, heat, and rating conditions for dl/lPAG [D] and vlPAG [E]. Significant findings ($p<0.05$) are demarcated by the asterisks (*). dl/l, dorsolateral/lateral; vl, ventrolateral; PAG, periaqueductal gray. (For interpretation of the references to color in this figure legend, the reader is referred to the web version of this article.)

C1. Static functional connectivity during resting state scans. dl/l and vlPAG have different static functional connectivity profiles during resting-state scans. During resting state fMRI scans, the dl/lPAG showed significantly higher functional connectivity with left and right thalamus (Thal_L, Thal_R; $p<0.001$). In contrast, relative to dl/lPAG, the vlPAG showed greater functional connectivity with right and left posterior divisions of the parahippocampal gyrus (pHippp_R, pHippp_L; $p<0.001$, result not illustrated).

C2. Static functional connectivity during pain task scans. Static functional connectivity averaged for the three pain task scans demonstrated that the dl/lPAG and vlPAG preferentially connect to distinct networks (Fig. 5 and Table 2). The dl/lPAG preferentially connected to the salience network with regions such as the right rostral anterior cingulate cortex (ACCr_R), left and right rostral mid-posterior ACC (ACCrm_L, ACCrm_R), left rostral posterior ACC (ACCrp_L), left inferior frontal gyrus pars opercularis (IFGpo_L), left thalamus (Thal_L), right thalamus (Thal_R), and left dorsal anterior insula (dINSa_L).

Conversely, the vlPAG preferentially connected with regions involved in language and memory processing such as the right Heschl's gyrus (He_R), left hippocampus (Hipp_L), right anterior division of the superior temporal gyrus (STGa_R), left posterior division of the superior temporal gyrus (STGp_L), right anterior division of the parahippocampal gyrus (pHippa_R), and the left and posterior divisions of the parahippocampal gyrus (pHippp_L, pHippp_R). Significant results ($p<0.05$) are summarized below in Fig. 5 and Table 2.

C3. Time-varying functional connectivity (TVFC) during resting state and task scans. The TVFC measured from the resting state scan showed significant differences between dl/lPAG and vlPAG. The left rostral medial ACC (ACCrm_L), the left rostral posterior ACC (ACCrp_L), and the left posterior supramarginal gyrus (SMGp_L) showed greater TVFC with dl/lPAG than with vlPAG. In addition, the dl/lPAG showed greater TVFC with the left thalamus (Thal_L). On the other hand, the vlPAG showed higher connectivity with the right posterior parahippocampal gyrus (pHippp_R) than the dl/lPAG. Thus more regions were detected as significant when observed using TVFC relative to the static FC analysis (see result C1).

Time-varying functional connectivity averaged for the three pain task scans also demonstrated that dl/lPAG and vlPAG synchronized with other brain regions in a distinct manner (Fig. 6, Table 3). Thus, when the TVFC was averaged for dl/lPAG and vlPAG matrices for the three task scans and were statistically compared and corrected for multiple correction, several regions were observed to be significant. As was observed with the static functional connectivity analysis on task scans, the dl/lPAG preferentially connected to the salience network at more instances relative to the vlPAG. These were regions such as the left dorsal anterior insula (dINSa_L), left and right inferior frontal gyrus pars opercularis (IFGpo_L, IFGpo_R), right mid anterior cingulate (ACCm_R), left and right rostral anterior cingulate (ACCr_L, ACCr_R), left and right rostral anterior cingulate mid-posterior (ACCrm_L, ACCrm_R), left and right rostral anterior cingulate posterior (ACCrp_L, ACCrp_R), and left and right thalamus (Thal_L, Thal_R). The TVFC also showed some regions that were not detected when measuring static FC. For instance, several regions with the supramarginal gyrus (Table 3), the temporal pole (TP), the putamen and the superior frontal gyrus also showed to synchronize with the dl/lPAG relatively more than vlPAG.

In contrast, the vlPAG preferentially connected with regions implicated in memory, semantic processing, and sensory processing. Effects were observed for regions such as left and right hippocampus (Hipp_L, Hipp_R), right mid temporal gyrus anterior division (MTGa_R), left and right mid temporal gyrus posterior division (MTGp_L, MTGp_R), right parahippocampal gyrus anterior division (pHippa_R), left and right parahippocampal gyrus posterior division (pHippp_L, pHippp_R), left and right temporal fusiform cortex posterior division (TFCp_L, TFCp_R), left temporal occipital cortex (TOF_L), left and right central opercular

Table 1
Differences in dl/l and vlPAG functional connectivity profiles between high and low threat conditions, shown with T-stat and P-values. After correcting for multiple comparisons, all findings were significant at $p<0.05$. dl/l, dorsolateral/lateral; vl, ventrolateral; PAG, periaqueductal gray; L, left; R, right.

Region of interest (condition)	MNI coordinates (x, y, z)	*T*-stat value	*P*-value
vlPAG (high threat ≥ low threat)			
L globus pallidus (GP_L)	−16, −2, −2	2.9348	0.0059
L posterior insula (INSp_L)	−38, −14, 8	3.231	0.0027
R globus pallidus (GP_R)	16, −2, −2	3.4072	0.0017
R middle insula (INSm_R)	40, −2, −2	3.4382	0.0015
R thalamus (Thal_R)	10, −18, 8	3.5646	0.0011
L dorsal anterior insula (dINSa_L)	−32, 20, 0	3.5787	0.0010
L rostral anterior cingulate mid-posterior (ACCrm_L)	20, 28, 18	3.7883	0.0006
R anterior cingulate posterior (ACCrp_R)	−6, −2, 42	3.9545	0.0004
R rostral anterior cingulate mid-posterior (ACCrm_R)	−6, 60, 80	4.8125	<0.001
R anterior cingulate posterior (ACCrp_L)	6, 18, −34	5.2079	<0.001
vlPAG (low threat ≥ high threat)			
L anterior middle temporal gyrus (MTGa_L)	−58, −2, −22	−3.245	0.0026
L amygdala (Amyg_L)	−24, −4, −18	−3.1981	0.0029
R frontal orbital cortex (FO_R)	40, 20, 4	−3.1849	0.0030
R medial prefrontal cortex (MPFC_R)	6, 60, 8	−3.1184	0.0036
R anterior middle temporal gyrus (MTGa_R)	58, −2, −22	−3.081	0.0040
L medial prefrontal cortex (MPFC_L)	−6, 60, 8	−3.039	0.0045
R middle frontal gyrus (MFG_R)	40, 20, 44	−3.01	0.0048
dl/lPAG (high threat ≥low threat)			
R rostral anterior cingulate mid-posterior (ACCrm_R)	−6, 60, 8	3.6648	0.0008
L anterior cingulate posterior (ACCrp_L)	6, 18, 34	4.0591	0.0003
dl/lPAG (low threat ≥high threat)			
R anterior middle temporal gyrus (MTGa_R)	58, −2, −22	−3.7628	0.0006
L anterior middle temporal gyrus (MTGa_L)	−58, −2, −22	−3.4434	0.0015

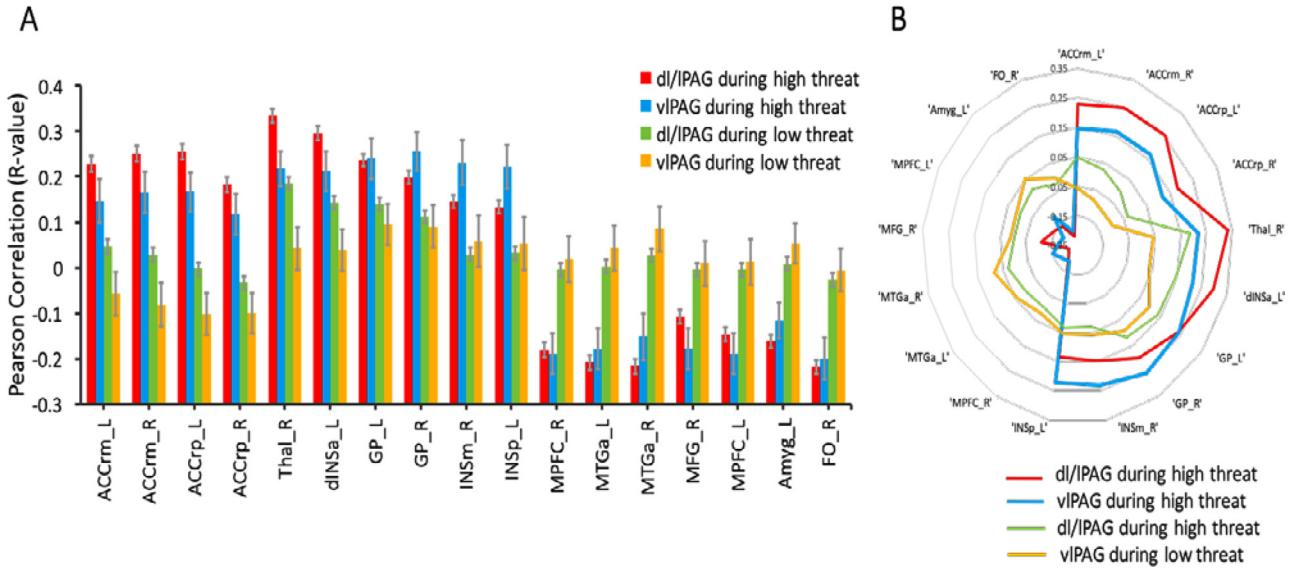

Fig. 4. Overlapping and distinct connectivity profiles with changes in task conditions (high threat and low threat). vlPAG showed a change in synchrony with a larger number of regions than dl/lPAG between high threat and low threat conditions. [A] dl/lPAG (red) and vlPAG (blue) were synchronized positively with anterior cingulate regions, thalamus, globus pallidus, and insular regions and negatively with middle temporal, medial and lateral prefrontal, amygdala, and fronto-orbital regions during the high threat condition. During the low threat condition, the coupling of vlPAG and dl/lPAG with several regions was reduced. For significance values, see Table 1. [B] When observed as a polar chart, the data shows distinctions between dl/l and vlPAG both within and between conditions but the differences did not survive FDR correction. dl/l, dorsolateral/lateral; vl, ventrolateral; PAG, periaqueductal gray; L, left; R, right; GP_L, left globus pallidus; ACCrp_R, right rostral posterior anterior cingulate cortex; Thal_R, right thalamus; dINSa_L, left dorsal anterior insula; INSp_L, left posterior insula; MFG_R, right middle frontal gyrus; ACCrm_L, left rostral mid-posterior ACC; ACCrm_R, right ACCrm; ACCrp_L, left ACCrp; GP_R, right globus pallidus; INSm_R, right middle insula; MPFC_R; right medial prefrontal cortex; MTGa_L, left anterior middle temporal gyrus; MTGa_R, right MTGa; MPFC_L, left MPFC; Amyg_L, left amygdala; FO_R, right frontal orbital cortex. (For interpretation of the references to color in this figure legend, the reader is referred to the web version of this article.)

cortex (Cop_L, Cop_R), and left and right Heschl's gyrus (He_L, He_R). Significant results ($p<0.05$) are summarized below in Fig. 6 and Table 3. While some regions detected were similar to those found with the static FC analysis, the TVFC analysis detected a significantly higher number of regions. But most regions connected with vlPAG were within the temporal lobe and the insula.

To illustrate how often dl/l and vlPAG change their affiliations with other regions during different time windows, we have depicted the shifts for a few regions in Fig. 7, separated for the three task scans. Note that dl/lPAG connectivity with components of the salience network (anterior insula and right rostral mid cingulate) fluctuates throughout the scans, and remains significantly higher than the vl-

Table 2
Preferential dl/l and vlPAG static functional connectivity profiles during pain task scans, shown with T-stat and P-values. All findings were significant at $p<0.05$. dl/l, dorsolateral/lateral; vl, ventrolateral; PAG, periaqueductal gray; L, left; R, right.

Region of interest (condition)	MNI coordinates (x, y, z)	*T*-stat value	*P*-value
dl/lPAG≥vlPAG			
R Rostral Anterior Cingulate (ACCr_R)	2, 28, 18	−3.0888	0.0039
L Rostral Anterior Cingulate Mid-Posterior *(ACCrm_L)*	20, 28, 18	−3.5294	0.0012
R Rostral Anterior Cingulate Mid-Posterior *(ACCrm_R)*	−6, 60, 8	−3.584	0.001
L Rostral Anterior Cingulate Posterior (ACCrp_L)	6, 18, 34	−2.9752	0.0053
L Inferior Frontal Gyrus, pars opercularis *(IFGpo_L)*	−54, −20, 46	−3.5708	0.0011
L Thalamus *(Thal_L)*	−10, −18, 8	−4.5847	0.0001
R Thalamus *(Thal_R)*	10, −18, 8	−4.4362	0.0001
L Dorsal Anterior Insula (dINSa_L)	−32, 20, 0	−2.8177	0.0079
R Rostral Anterior Cingulate	2, 28, 18	−3.0888	0.0039
vlPAG≥dl/lPAG			
R Heschl's Gyrus, includes H1 and H2 (He_R)	48, −18, −6	3.7755	0.0006
L Hippocampus (Hipp_L)	−28, −22, −16	3.731	0.0007
R Superior Temporal Gyrus, anterior division (STGa_R)	58, −4, −6	2.8748	0.0068
L Superior Temporal Gyrus, posterior division (STGp_L)	−66, −26, 6	3.0621	0.0042
R Parahippocampal Gyrus, anterior division (pHippa_R)	34, −6, −34	4.223	0.0002
L Parahippocampal Gyrus, posterior division (pHippp_L)	−34, −32, −18	5.7044	>0.0001
R Parahippocampal Gyrus, posterior division (pHippp_R)	34, −32, −18	4.3973	0.0001

Table 3
Preferential dl/l and vlPAG time-varying functional connectivity profiles during pain task scans, shown with *T*-stat and *P*-values. All findings were significant at $p<0.05$. dl/l, dorsolateral/lateral; vl, ventrolateral; PAG, periaqueductal gray; L, left; R, right.

Region of interest (condition)	MNI coordinates (x, y, z)	*T*-stat value	*P*-value
dl/lPAG≥vlPAG			
R Mid Anterior Cingulate (ACCm_R)	6, −2, 42	2.6178	0.013
L Rostral Anterior Cingulate (ACCr_L)	−4, 38, 18	3.1941	0.003
R Rostral Anterior Cingulate (ACCr_R)	4, 38, 18	3.9376	0.0004
L Rostral Anterior Cingulate Mid-Posterior (ACCrm_L)	−6, 18, 34	4.7721	>0.0001
R Rostral Anterior Cingulate Mid-Posterior (ACCrm_R)	6, 18, 34	5.3995	>0.0001
L Rostral Anterior Cingulate Posterior (ACCrp_L)	−4, 22, 20	5.3375	>0.0001
R Rostral Anterior Cingulate Posterior (ACCrp_R)	4, 22, 20	2.9752	0.0053
L Inferior Frontal Gyrus pars opercularis (IFGpo_L)	−54, 14, 16	3.8587	0.0005
R Inferior Frontal Gyrus pars opercularis (IFGpo_R)	54, 14, 16	3.1253	0.0036
L Putamen (Put_L)	−30, −4, 0	2.7746	0.0088
R Putamen (Put_R)	30, −4, 0	2.8436	0.0074
L Superior Frontal Gyrus (SFG_L)	−22, 22, 54	2.5349	0.0159
L Supramarginal Gyrus, anterior division (SMGa_L)	−58, −32, 40	3.1481	0.0034
R Supramarginal Gyrus, anterior division (SMGa_R)	58, −32, 40	3.3259	0.0021
L Supramarginal Gyrus, posterior division (SMGp_L)	−60, −48, 32	3.0414	0.0044
R Supramarginal Gyrus, posterior division (SMGp_R)	60, −48, 32	2.438	0.02
R Temporal Pole (TP_R)	40, 16, −30	4.9589	>0.0001
L Thalamus (Thal_L)	−10, −18, 8	6.9441	>0.0001
R Thalamus (Thal_R)	10, −18, 8	7.0482	>0.0001
L Dorsal Anterior Insula (dINSa_L)	−32, 20, 0	4.7246	>0.0001
vlPAG≥dl/lPAG			
L Central Opercular Cortex (Cop_L)	−48, −4, 8	−2.5253	0.0162
R Central Opercular Cortex (Cop_R)	48, −4, 8	−2.6475	0.0121
L Heschls Gyrus (He_L)	−48, −18, 6	−2.4575	0.0191
R Heschls Gyrus (He_R)	48, −18, 6	−4.8215	>0.0001
L Hippocampus (Hipp_L)	−28, −22, −16	−5.4375	>0.0001
R *Hippocampus* (Hipp_R)	28, −22, −16	−2.4996	0.0173
R Middle Temporal Gyrus, anterior division (MTGa_R)	58, −2, −22	−3.2321	0.0027
L Middle Temporal Gyrus, posterior division (MTGp_L)	−62, −22, −18	−4.787	>0.0001
R Middle Temporal Gyrus, posterior division (MTGp_R)	62, −22, −18	−4.1574	0.0002
L Middle Temporal Gyrus, temporooccipital part (MTGto_L)	−60, −52, 0	−2.5407	0.0157
R Planum Polare (PlP_R)	48, −4, −6	−2.3403	0.0251
L Planum Temporale (PlT_L)	−60, −22, 8	−2.4843	0.0179
L Superior Temporal Gyrus, anterior division (STGa_L)	−58, −4, −6	−3.0304	0.0046
R Superior Temporal Gyrus, anterior division (STGa_R)	58, −4, −6	−4.4675	0.0001
L Superior Temporal Gyrus, posterior division (STGp_L)	−66, −26, 6	−5.0925	>0.0001
R Superior Temporal Gyrus, posterior division (STGp_R)	66, −26, 6	−2.5882	0.014
L Temporal Fusiform Cortex, posterior division (TFCp_L)	−36, −16, −32	−2.5969	0.0137
R Temporal Fusiform Cortex, posterior division (TFCp_R)	36, −16, −32	−3.5708	0.0011
L Temporal Occipital Fusiform Cortex (TOF_L)	−34, −54, −16	−2.8268	0.0077
R Parahippocampul Gyrus, anterior division (pHippa_R)	24, −6, −34	−5.2468	>0.0001
L Parahippocampul Gyrus, posterior division (pHippp_L)	−24, −32, −18	−7.9587	>0.0001
R Parahippocampul Gyrus, posterior division (pHippp_R)	24, −32, −18	−4.9416	>0.0001

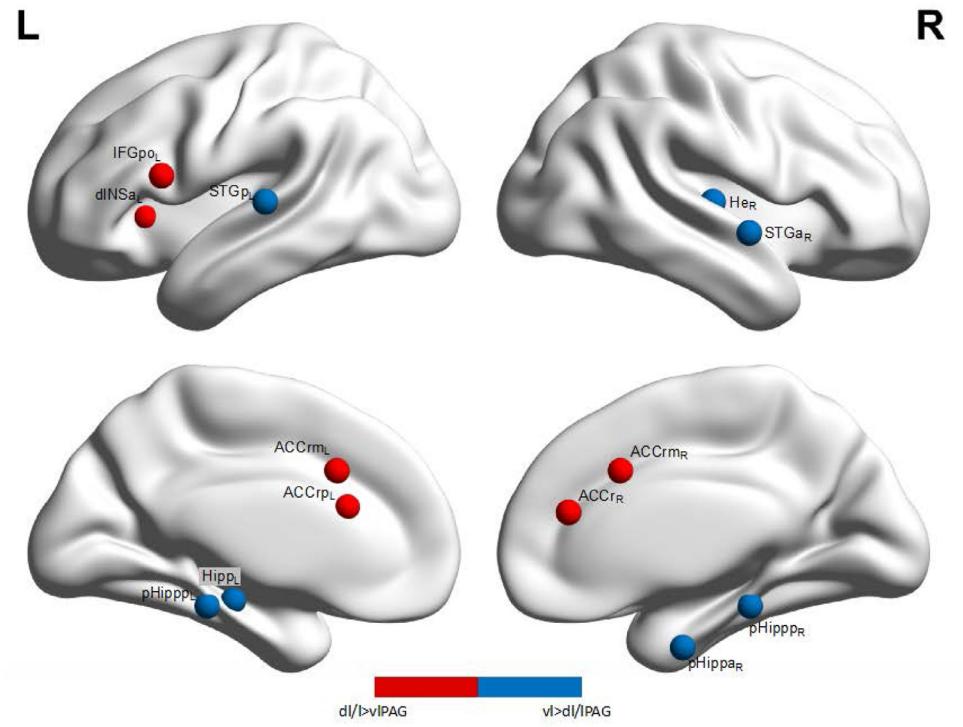

Fig. 5. Static functional contrast connectivity profiles of the dl/l and vlPAG during task-scans. The dl/lPAG preferentially connects to IFGpo_L, Thal_L, dINSa_L, ACCrm_R, ACCrp_L, ACCrm_L, and Thal_R. The vlPAG preferentially connects to STGp_L, pHippp_L, Hipp_L, STGa_R, pHippa_R, and pHippp_R. After correcting for multiple comparisons, all findings were significant at $p<0.05$. dl/l, dorsolateral/lateral; vl, ventrolateral; PAG, periaqueductal gray; IFGpo_L, left inferior frontal gyrus, pars opercularis; Thal_L, left thalamus; dINSa_L, left dorsal anterior insula; ACCrm_R, right rostral anterior cingulate cortex; ACCrp_L, left posterior ACC; ACCrm_L, left mid-posterior ACC; Thal_R, right thalamus; STGp_L, left posterior division of the superior temporal gyrus; pHippp_L, left posterior division of the parahippocampal gyrus; Hipp_L, left hippocampus; STGa_R, right anterior division of the superior temporal gyrus; pHippa_R, right anterior division of the parahippocampal gyrus; pHippp_R, right posterior division of the parahippocampal gyrus; L, left; R, right.

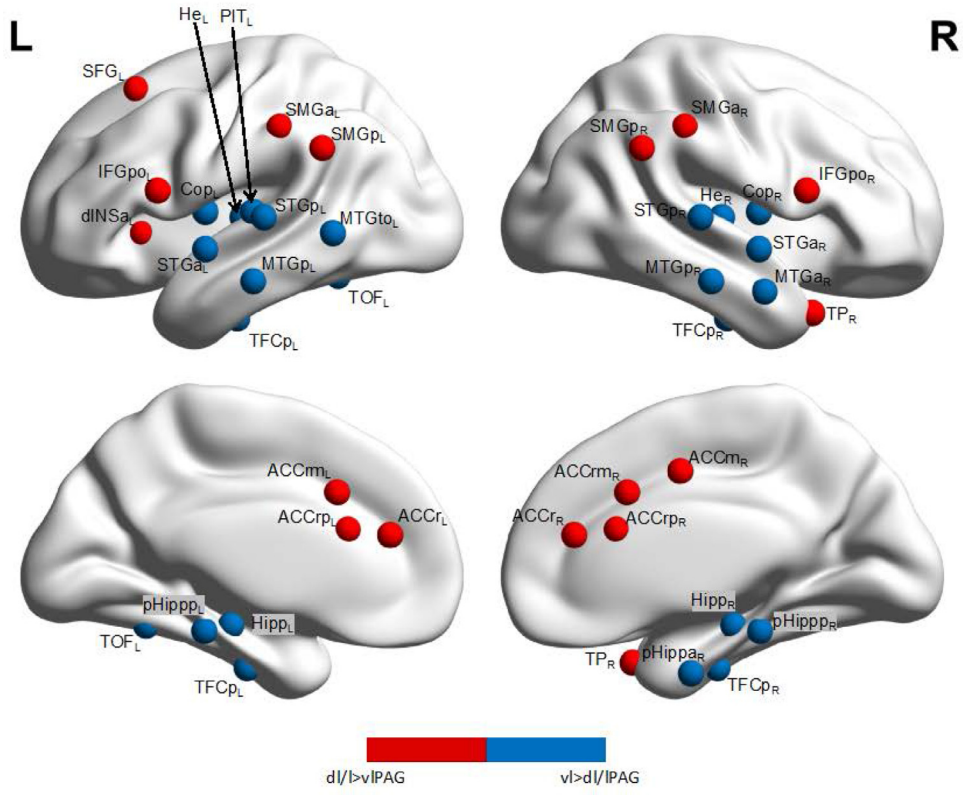

Fig. 6. Time-varying functional connectivity during pain task scans. The regions that on average connected more with dl/lPAG more frequently on a moment to moment basis (assessed using a sliding window analysis) relative to vlPAG are shown in red. The opposite contrast vlPAG> dl/lPAG is shown in blue. FDR corrected, $p<0.05$.

PAG connectivity with these regions. In addition, we selected a sensory (left central operculum, S2) and a memory region (hippocampus) to illustrate vlPAG favoring those regions. Both dl/lPAG and vlPAG connected with the S2 region, but vlPAG connectivity was frequently higher than dl/lPAG at several points at a statistically significant level. In comparison, the vlPAG relative to dl/lPAG connectivity with the hippocampus was significantly stronger during most time points.

C4. Brain wide connectivity (degree) of vlPAG is higher than dl/lPAG during resting state and task scans. There was no significant difference between dl/lPAG and vlPAG in the averaged degree (brain wide connections) in the resting state scan when static func-

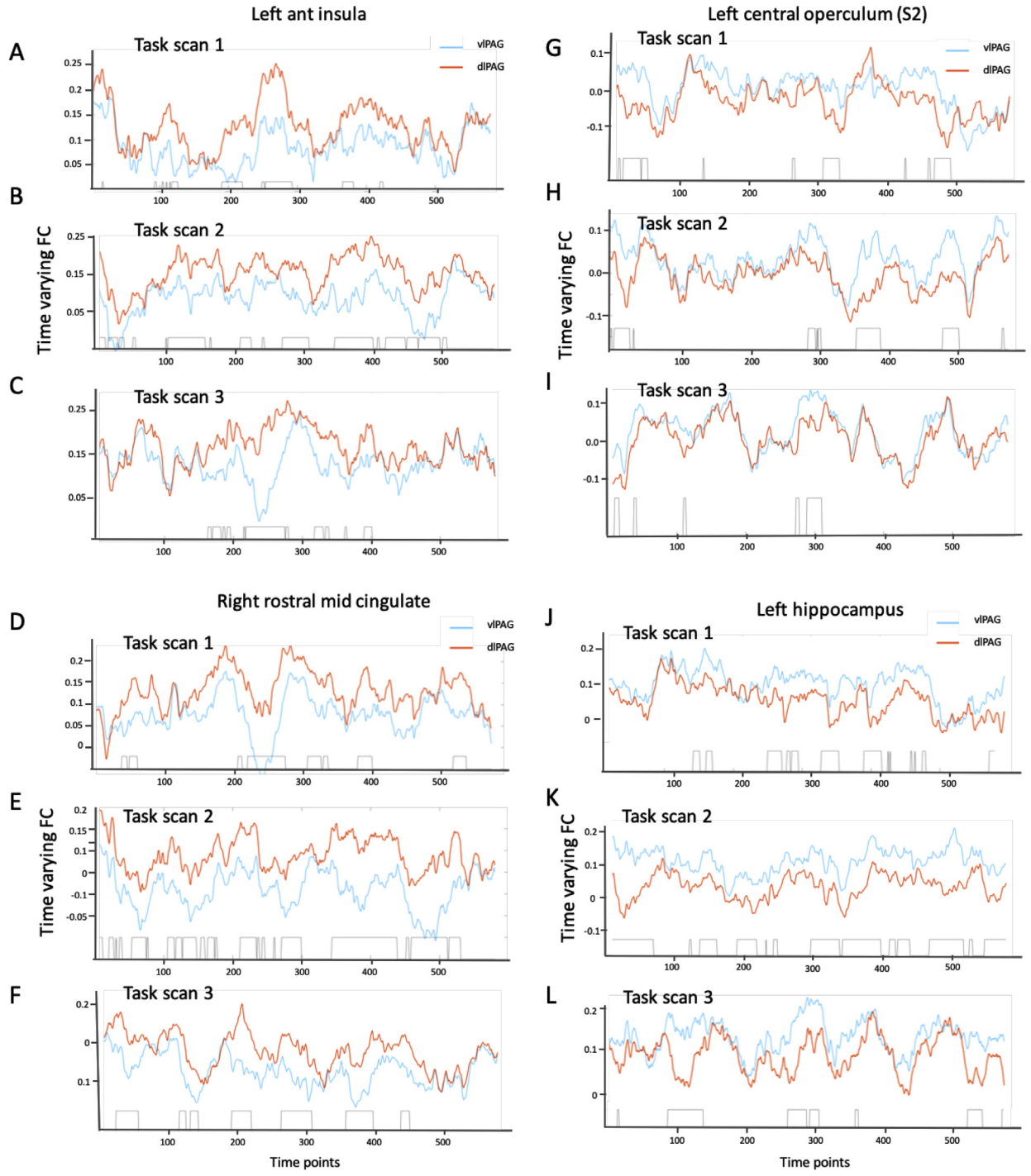

Fig. 7. Comparison of time-varying functional connectivity of dl/l and vlPAG in various brain regions during pain task scans. Black boxes along the X-axis signify a statistically significant difference ($p<0.05$) between vl and dl/lPAG TVFC. Top left: comparison of TVFC of dl/l and vlPAG in the left dorsal anterior insula during [A] pain task scan 1, [B] pain task scan 2, and [C] pain task scan 3. Bottom left: comparison of time varying FC of dl/land vlPAG in the right rostral anterior cingulate mid-posterior during [D] pain task scan 1, [E] pain task scan 2, and [F] pain task scan 3. Top right: comparison of time varying FC of dl/land vlPAG in the left central opercular cortex (S2) during [G] pain task scan 1, [H] pain task scan 2, and [I] pain task scan 3. Bottom right: comparison of time varying FC of dl/land vlPAG in the left hippocampus during [J] pain task scan 1, [K] pain task scan 2, and [L] pain task scan 3. dl, dorsolateral; vl, ventrolateral; PAG, periaqueductal gray; FC, functional connectivity.

tional connectivity matrices were employed ($p>0.05$). Similarly, the degree values from time-varying functional connectivity for different windows or when averaged in the resting state scan were not significantly different between dl/lPAG and vlPAG (Fig. 8A & E). However, during task scans, vlPAG appeared to be connected to significantly more brain regions than the dl/lPAG (Fig. 8B-D & F). Thus, as shown in Figures B-D, the vlPAG showed connectivity with significantly more regions relative to dl/lPAG for several windows of time. The effects were strongest for the first test scan (B). The degree value averaged for all three scans was significantly higher for the vlPAG relative to dl/lPAG (F).

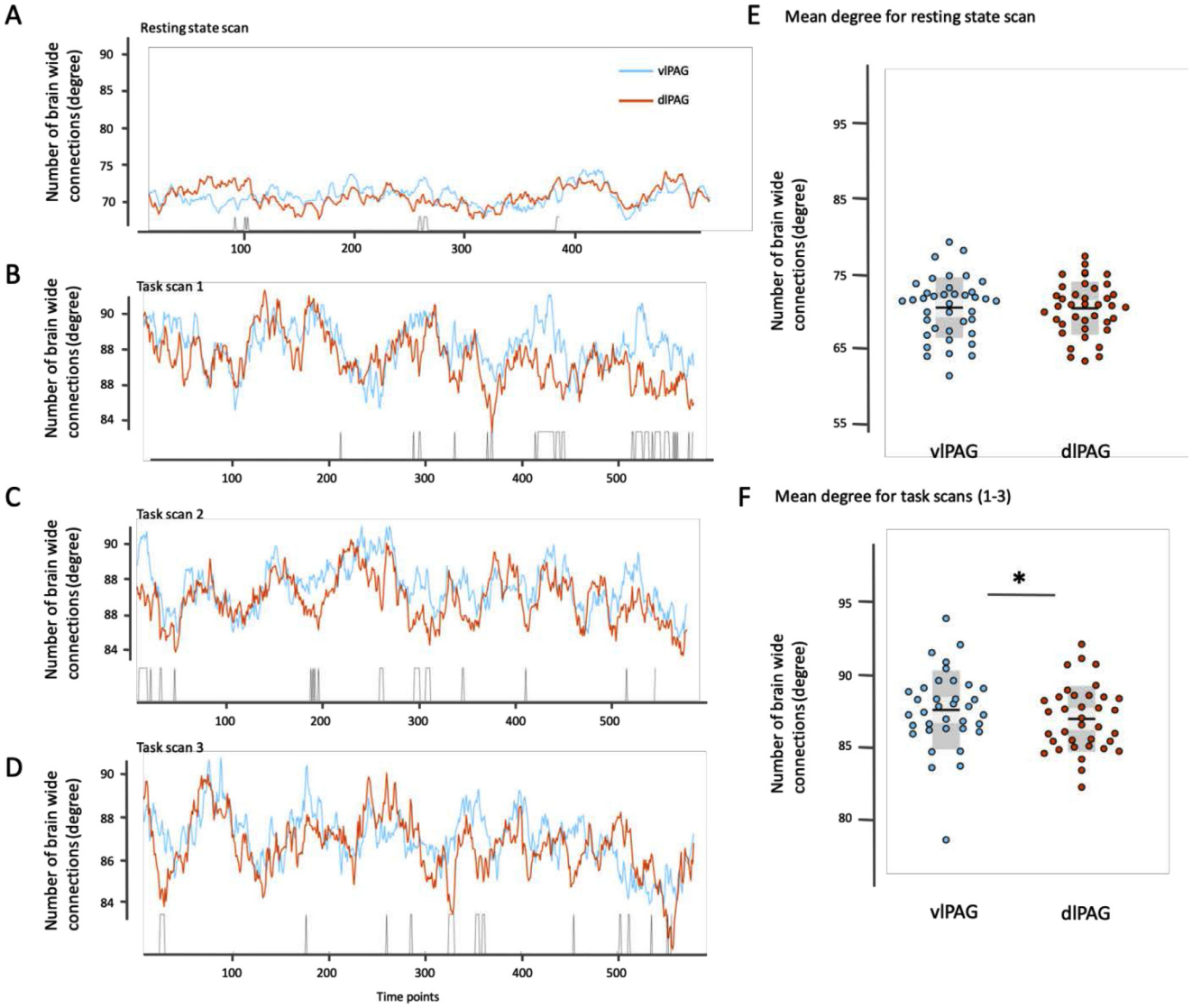

Fig. 8. Comparison of dl/l and vlPAG brain wide connections (degree) measured in time-varying functional connectivity data. [A] Number of brain wide connections (degree) for dl/l and vlPAG in time-varying FC in resting state scan. [B] Number of brain wide connections (degree) for dl/l and vlPAG in time-varying FC in pain task scan 1. [C] Number of brain wide connections (degree) for dl/l and vlPAG in time-varying FC in pain task scan 2. [D] Number of brain wide connections (degree) for dl/l and vlPAG in time-varying FC in pain task scan 3. [E] Mean number of brain wide connections (degree) for dl/l and vlPAG during resting scan. [F] Mean number of brain wide connections (degree) for dl/l and vlPAG averaged across pain task scans 1–3. Significant findings ($p<0.05$) are denoted by the asterisks (*). dl, dorsolateral; vl, ventrolateral; PAG, periaqueductal gray; FC, functional connectivity.

5. Discussion

This study establishes that the two PAG columns implicated in pain processing are responsive to the *threat* of experiencing pain. Their activation patterns indicate that these two regions are more responsive when the incoming noxious stimulus is expected to be high or when its intensity is unknown. Taken together, these two columns are involved in responding to the threat of receiving painful stimuli both with or without top-down expectation cues and respond less when less pain is expected. The two regions showed similar patterns of responses, and more experimentation is needed to disambiguate the specific contexts in which these two regions activate differently. While the activation patterns were similar, we noted differences in the functional connectivity patterns of the two studied PAG columns. First, they show consistent whole brain corrected differences in their functional connectivity profiles. The dl/lPAG consistently connects with the thalamus and salience networks and thus may have more involvement in vigilance, salience detection, and quick decisions. In contrast, the vlPAG connects to more regions in the brain and consistently connects with the memory/semantic processing regions. Thus, this region may be engaged in contextualizing threats. When viewed within existing frameworks of what is known about the function of these two regions in animal research, it appears that they may be components of distinct brain systems and have different functions in threat processing.

The PAG is an important node for top-down pain modulation. It has been noted that the PAG is an evolutionarily conserved region necessary for self-preservation. This region is also important for aversive learning through its connections with the amygdala (George et al., 2019; Johansen et al., 2010). The present study suggests that its main role is in regulating physical responses and sensory decisions in the face of a dynamic landscape of aversive and noxious events. This region is also implicated in regulating behavior and responses to threats and plays a critical role in pain processing (Benarroch, 2012; Linnman et al., 2012). The PAG is said to modulate pain through its interaction with descending top-down signals from the dlPFC and ACC (Scott et al., 2008; Peyron, 2014), but the specific mechanism through which the human

PAG participates in top-down pain modulation has remained ambiguous. Most of what is known about the role of the PAG in pain modulation is based on animal research. Human neuroimaging studies have so far suggested that PAG activations are observed in conditions when pain intensity is high relative to when it is low (Atlas et al., 2010; Fazeli and Buchel, 2018; Wager et al., 2013) and also during pain anticipation (Brodersen et al., 2012). The PAG is also implicated in treatment-related expectation effects where the precision of, or confidence in, the expected effectiveness of a treatment corresponds with an increase in activation of the PAG (Grahl et al., 2018). Moreover, two new studies (Lin et al., 2014; Seymour, 2019) have reported that higher activation in the PAG is associated with higher uncertainty about the experience of pain. Our findings merge these disparate findings by demonstrating that the dl/l and vlPAG respond to both stronger and uncertain threats of pain, while responding weakly to lower threats. Taken together with the present findings, the PAG appears to engage more in conditions that involve aversive aspects such as when expectations are negative, or uncertain, and when a strong pain stimulus is applied (Samineni et al., 2017; Huang et al., 2019; Faull et al., 2019).

Additionally, we report that the PAG activates in response to cued or uncued high intensity noxious events, but the overall response model was not significantly different between dl/lPAG and vlPAG. We also observed some notable differences in activation patterns of dl/l and vlPAG. For instance, relative to responses observed in vlPAG, the dl/lPAG was activated relatively more strongly during the rating period, especially within the high and unknown threat epochs. Moreover, vlPAG showed greater difference in activation during the heating and rating periods for HT vs LT conditions relative to dl/lPAG. Note that the vlPAG, relative to dl/lPAG, showed greater synchronization with somatosensory areas 1 and 2, and middle and posterior insula, in most functional connectivity analyses reported in this study. When taken together, the findings indicate a role for vlPAG in feedback and feedforward sensory circuits. In contrast, dl/lPAG synchronized relatively more with higher order sensory and multimodal regions such as the anterior insula, dorsal ACC, supramarginal gyrus, and inferior frontal gyrus. Hence, the dl/lPAG may be more involved in receiving top-down information required for making quick executive decisions on how to respond to threats. Animal studies have also indicated that the dl/lPAG is necessary for generating escape responses and for generating fight, flight, or fright responses through sympathetic activation (Lumb et al., 2002; Keay and Bandler, 2002; Kincheski et al., 2012; Mochny et al., 2013; Watson et al., 2016; Bandler et al., 2000). The vlPAG is implicated in inescapable responses to threat in rodents and the condition is said to be equivalent to situations that require the preparation of responses by processing information so that a more contextualized, albeit slower, response can be generated. Most of these assertions, however, are based on animal research. Higher-order human brain systems are more complex when it comes to threat processing. Interestingly, a recent study has also demonstrated that the vlPAG increases activation with increase in task demands in an N-back working memory task (Kragel et al., 2018). A robust analysis of data from several studies revealed that PAG activity was observed during aversion, situations of negative emotion (Harrison et al., 2010; George et al., 2019), and during respiratory distress (Faull et al., 2016; Faull et al., 2019). The convergence from these different lines of investigation indicates that the PAG's role is in monitoring and responding to cues that predict a high risk of distress and/or a need for self-preservation. In addition, the PAG's sensitivity to threat cues indicates its function in preparing a response to incoming threats, as suggested earlier (Mobbs et al., 2007; Wright et al., 2019; Wright and McDannald, 2019). New studies are needed that are specifically designed to disentangle the different functional roles of the two columns, with conceptual frameworks that bridge the fMRI-based findings and animal-based studies.

A parcellation-based connectomics approach toward functional connectivity demonstrably shows that the dl/lPAG is consistently synchronized with the salience network and the thalamus. The vlPAG also connects with the salience network, but this is relatively sporadic. The pertinent feature of vlPAG connectivity is that it has more widespread connections and frequently synchronizes with memory, language comprehension, semantic processing, and primary sensory regions. Since BOLD frequencies fluctuate in the infra-slow range, and are putatively important for synchronizing brain activity, the present findings are reflective of how brain-wide interactions mediate the integration of predictions and priors with bottom-up sensory inputs (Suarez et al., 2020; Seymour and Mancini, 2020). The different patterns of connectivity direct us to what is known from animal studies, which show that the vlPAG acts as a neurobiological substrate for goal-oriented responses to threats (LeDoux and Daw, 2018) and is important in threat contextualization such as freezing behavior (Roelofs, 2017; Fanselow and Kim, 1992). The involvement of the vlPAG in higher-order cognitive networks is consistent with vlPAG's function as a "breaker" in the dl/lPAG-sympathetic nervous system to prepare appropriate responses to threats (Roelofs, 2017; Tovote et al., 2016). vlPAG connectivity with posterior insula and dl/lPAG connectivity with anterior insula indicate the role of the posterior insula in computing and propagating prediction errors (Barrett and Simmons, 2015; Preuschoff et al., 2008) and the anterior insula in anticipatory activity (Atlas et al., 2010; Fenton et al., 2015; Fazeli and Buchel, 2018). Moreover, shifts in response from salience to higher-order cognitive networks was shown to mirror the switch between the sympathetic and parasympathetic systems during threats (Walker and Carrive, 2003; Eilam, 2005; Young et al., 2017). The dl/lPAG connectivity with the salience network was consistent across conditions and was even observed during the LT task synchronization, indicating that the dl/lPAG may be an intrinsic component of the salience network. The dl/lPAG activation patterns are also consistent with its proposed function in sympathetic arousal to threat (Roelofs, 2017) and fight, flight, or fright responses (LeDoux and Daw, 2018) and thus to threats demanding quicker responses (Lumb et al., 2002; Parry et al., 2008; Fanselow and Kim, 1992).

The main limitation of this study is that a higher spatial strength and temporal resolution (>0.5 s) is said to help with reducing effects of brainstem noise on data quality. In the absence of required resources, we selected a sampling rate/voxel size balance that increases temporal sampling rate without negatively impacting the signal to noise ratio (SNR). Multibanding at the moderate acceleration factors used in this study captures more information per unit time in task based fMRI (Chen et al., 2014) and increases sensitivity for detecting task responses and improves stability of resting state networks (Preibisch et al., 2015). A sampling rate at higher acceleration factors (>3) significantly drops the SNR (Daranyi et al., 2021). More research is needed to understand how the specific noise correction protocols and higher sampling rates influence fMRI activation results. As was discussed by Napadow , voxel-wise analyses to map activations in the brainstem is affected by the artifacts from cerebrospinal fluid in the aqueduct especially when cluster correction is used (Napadow et al., 2019). Moreover, the benchmarks for removing noise in multibanded signals are even less obvious. Hence, we focused on using data driven approaches to analyze data, and used multiple scans collected at a sampling rate that has less negative impact on SNR. In addition, this was a within subject, group-level design for comparing two adjacent regions in the brainstem. Moreover, the whole brain coverage allowed us to study brain wide functional connectivity.

Note that we relied on a data driven approach of extracting time series from defined anatomical regions. The extracted time series were juxtaposed on the event timings (a decoding approach) (Upadhyay et al., 2010) and the activations were confirmed to be visually and statistically obvious. The activations in the control brainstem region did not show a significant difference between the task conditions. In addition, we took the necessary precautions of removing noise artifacts during preprocessing and assured that the data quality was reliable by detecting participants with high head movement with motion outlier detection.

The functional connectivity patterns somewhat diverge from a few previous studies that used resting state data (Ezra et al., 2015;

Kong et al., 2010). This is the first study that demonstrates within-subject reproducibility using different types of scans (resting state and three pain task scans) and techniques (time-varying and static functional connectivity) with high-resolution, multibanded repetitions.

In conclusion, the PAG is a system of regions that mediate responses to actual and potential noxious events. The most consistent and notable finding from the series of investigations is that (1) the dl/lPAG is a key component of the salience network, and (2) vlPAG connectivity is indicative of its function in semantic and memory-based contextualization of threats. Taken together with what is known from animal studies, this study suggests that the dl/lPAG and the vlPAG are important nodes for processing the threat of pain, while performing distinct functions in integrating bottom-up and top-down information from different parts of the brain, such that noxious events can be appraised and responded to in a context-specific manner.

Credit authorship contribution statement

Sean Wang: Conceptualization, Data curation, Formal analysis, Investigation, Methodology, Resources, Software, Visualization, Writing – original draft. **Jennika Veinot:** Methodology, Resources, Software, Visualization, Writing – original draft. **Amita Goyal:** Data curation. **Ali Khatibi:** Project administration, Validation, Writing – review & editing. **Sara W. Lazar:** Investigation, Project administration, Validation, Writing – review & editing. **Javeria Ali Hashmi:** Supervision, Conceptualization, Data curation, Formal analysis, Funding acquisition, Investigation, Methodology, Project administration, Resources, Software, Validation, Writing – original draft, Writing – review & editing.

Acknowledgments

NSERC Discovery Grant, Canada Research Chairs Program, Canadian Institute of health Research (CIHR) Project Grant. John R. Evans Leaders and Canada Innovation Funds (CFI-JELF), Nova Scotia Health Authority (NSHA) Establishment Grant and NSHA Fibromyalgia Research Grant.

Supplementary materials

Supplementary material associated with this article can be found, in the online version, at doi:10.1016/j.neuroimage.2022.118936.

References

Atlas, L.Y., Bolger, N., Lindquist, M.A., Wager, T.D., 2010. Brain mediators of predictive cue effects on perceived pain. J. Neurosci. 30 (39), 12964–12977.
Bandler, R., Keay, K.A., Floyd, N., Price, J., 2000. Central circuits mediating patterned autonomic activity during active vs. passive emotional coping. Brain Res. Bull. 53 (1), 95–104.
Barrett, L.F., Simmons, W.K., 2015. Interoceptive predictions in the brain. Nat. Rev. Neurosci. 16 (7), 419–429.
Basbaum, A.I., Fields, H.L., 1984. Endogenous pain control systems: brainstem spinal pathways and endorphin circuitry. Annu. Rev. Neurosci. 7, 309–338.
Benarroch, E.E., 2012. Periaqueductal gray: an interface for behavioral control. Neurology 78 (3), 210–217.
Bouton, M.E., Bolles, R.C., 1979. Role of conditioned contextual stimuli in reinstatement of extinguished fear. J. Exp. Psychol. Anim. Behav. Process. 5 (4), 368–378.
Brodersen, K.H., Wiech, K., Lomakina, E.I., Lin, C.S., Buhmann, J.M., Bingel, U., Ploner, M., Stephan, K.E., Tracey, I., 2012. Decoding the perception of pain from fMRI using multivariate pattern analysis. Neuroimage 63 (3), 1162–1170.
Calhoun, V.D., Miller, R., Pearlson, G., Adali, T., 2014. The chronnectome: time-varying connectivity networks as the next frontier in fMRI data discovery. Neuron 84 (2), 262–274.
Carrive, P., 1993. The periaqueductal gray and defensive behavior: functional representation and neuronal organization. Behav. Brain Res. 58 (1–2), 27–47.
Carrive, P., Leung, P., Harris, J., Paxinos, G., 1997. Conditioned fear to context is associated with increased Fos expression in the caudal ventrolateral region of the midbrain periaqueductal gray. Neuroscience 78 (1), 165–177.
Chen, G., Adleman, N.E., Saad, Z.S., Leibenluft, E., Cox, R.W., 2014. Applications of multivariate modeling to neuroimaging group analysis: a comprehensive alternative to univariate general linear model. Neuroimage 99, 571–588.
Coulombe, M.A., Erpelding, N., Kucyi, A., Davis, K.D., 2016. Intrinsic functional connectivity of periaqueductal gray subregions in humans. Hum. Brain Mapp. 37 (4), 1514–1530.
Daranyi, V., Hermann, P., Homolya, I., Vidnyanszky, Z., Nagy, Z., 2021. An empirical investigation of the benefit of increasing the temporal resolution of task-evoked fMRI data with multi-band imaging. MAGMA 34 (5), 667–676.
Eilam, D., 2005. Die hard: a blend of freezing and fleeing as a dynamic defense–implications for the control of defensive behavior. Neurosci. Biobehav. Rev. 29 (8), 1181–1191.
Ezra, M., Faull, O.K., Jbabdi, S., Pattinson, K.T., 2015. Connectivity-based segmentation of the periaqueductal gray matter in human with brainstem optimized diffusion MRI. Hum. Brain Mapp. 36 (9), 3459–3471.
Fadok, J.P., Krabbe, S., Markovic, M., Courtin, J., Xu, C., Massi, L., Botta, P., Bylund, K., Muller, C., Kovacevic, A., et al., 2017. A competitive inhibitory circuit for selection of active and passive fear responses. Nature 542 (7639), 96–100.
Fanselow, M.S., Kim, J.J., 1992. The benzodiazepine inverse agonist DMCM as an unconditional stimulus for fear-induced analgesia: implications for the role of GABAA receptors in fear-related behavior. Behav. Neurosci. 106 (2), 336–344.
Faull, O.K., Jenkinson, M., Ezra, M., Pattinson, K., 2016. Conditioned respiratory threat in the subdivisions of the human periaqueductal gray. Elife 5.
Faull, O.K., Subramanian, H.H., Ezra, M., Pattinson, K.T.S., 2019. The midbrain periaqueductal gray as an integrative and interoceptive neural structure for breathing. Neurosci. Biobehav. Rev. 98, 135–144.
Fazeli, S., Buchel, C., 2018. Pain-Related Expectation and Prediction Error Signals in the Anterior Insula Are Not Related to Aversiveness. J. Neurosci. 38 (29), 6461–6474.
Fenton, B.W., Shih, E., Zolton, J., 2015. The neurobiology of pain perception in normal and persistent pain. Pain Manage. 5 (4), 297–317.
Fields, H.L., 2018. How expectations influence pain. Pain 159 (1), S3–S10 Suppl.
George, D.T., Ameli, R., Koob, G.F., 2019. Periaqueductal Gray Sheds Light on Dark Areas of Psychopathology. Trends Neurosci. 42 (5), 349–360.
Gibbons, A., 1985. Algorithmic Graph Theory. Cambridge University Press, New York Cambridge Cambridgeshire.
Grahl, A., Onat, S., Buchel, C., 2018. The periaqueductal gray and Bayesian integration in placebo analgesia. Elife 7.
Harrison, N.A., Gray, M.A., Gianaros, P.J., Critchley, H.D., 2010. The embodiment of emotional feelings in the brain. J. Neurosci. 30 (38), 12878–12884.
Hashmi, J.A., Baliki, M.N., Huang, L., Baria, A.T., Torbey, S., Hermann, K.M., Schnitzer, T.J., Apkarian, A.V., 2013. Shape shifting pain: chronification of back pain shifts brain representation from nociceptive to emotional circuits. Brain 136 (Pt 9), 2751–2768.
Hashmi, J.A., Kong, J., Spaeth, R., Khan, S., Kaptchuk, T.J., Gollub, R.L., 2014. Functional network architecture predicts psychologically mediated analgesia related to treatment in chronic knee pain patients. J. Neurosci. 34 (11), 3924–3936.
Hashmi, J.A., Loggia, M.L., Khan, S., Gao, L., Kim, J., Napadow, V., Brown, E.N., Akeju, O., 2017. Dexmedetomidine disrupts the local and global efficiencies of large-scale brain networks. Anesthesiology 126 (3), 419–430.
Heinricher, M.M., Tavares, I., Leith, J.L., Lumb, B.M., 2009. Descending control of nociception: specificity, recruitment and plasticity. Brain Res. Rev. 60 (1), 214–225.
Huang, J., Gadotti, V.M., Chen, L., Souza, I.A., Huang, S., Wang, D., Ramakrishnan, C., Deisseroth, K., Zhang, Z., Zamponi, G.W., 2019. A neuronal circuit for activating descending modulation of neuropathic pain. Nat. Neurosci. 22 (10), 1659–1668.
Johansen, J.P., Tarpley, J.W., LeDoux, J.E., Blair, H.T., 2010. Neural substrates for expectation-modulated fear learning in the amygdala and periaqueductal gray. Nat. Neurosci. 13 (8), 979–986.
Julius, D., Basbaum, A.I., 2001. Molecular mechanisms of nociception. Nature 413 (6852), 203–210.
Keay, K.A., Bandler, R., 2002. Distinct central representations of inescapable and escapable pain: observations and speculation. Exp. Physiol. 87 (2), 275–279.
Keay, K.A., Crowfoot, L.J., Floyd, N.S., Henderson, L.A., Christie, M.J., Bandler, R., 1997. Cardiovascular effects of microinjections of opioid agonists into the 'Depressor Region' of the ventrolateral periaqueductal gray region. Brain Res. 762 (1–2), 61–71.
Kincheski, G.C., Mota-Ortiz, S.R., Pavesi, E., Canteras, N.S., Carobrez, A.P., 2012. The dorsolateral periaqueductal gray and its role in mediating fear learning to life threatening events. PLoS ONE 7 (11), e50361.
Kong, J., Tu, P.C., Zyloney, C., Su, T.P., 2010. Intrinsic functional connectivity of the periaqueductal gray, a resting fMRI study. Behav. Brain Res. 211 (2), 215–219.
Koutsikou, S., Apps, R., Lumb, B.M., 2017. Top down control of spinal sensorimotor circuits essential for survival. J. Physiol. 595 (13), 4151–4158.
Kragel, P.A., Kano, M., Van Oudenhove, L., Ly, H.G., Dupont, P., Rubio, A., Delon–Martin, C., Bonaz, B.L., Manuck, S.B., Gianaros, P.J., et al., 2018. Generalizable representations of pain, cognitive control, and negative emotion in medial frontal cortex. Nat. Neurosci. 21 (2), 283–289.
LeDoux, J., Daw, N.D., 2018. Surviving threats: neural circuit and computational implications of a new taxonomy of defensive behaviour. Nat. Rev. Neurosci. 19 (5), 269–282.
Liao, C.H., Worsley, K.J., Poline, J.B., Aston, J.A., Duncan, G.H., Evans, A.C., 2002. Estimating the delay of the fMRI response. Neuroimage 16 (3), 593–606 Pt 1.
Lim, M., O'Grady, C., Cane, D., Goyal, A., Lynch, M., Beyea, S., Hashmi, J.A., 2020. Threat Prediction from Schemas as a Source of Bias in Pain Perception. J. Neurosci. 40 (7), 1538–1548.
Lin, C.S., Hsieh, J.C., Yeh, T.C., Niddam, D.M., 2014. Predictability-mediated pain modulation in context of multiple cues: an event-related fMRI study. Neuropsychologia 64, 85–91.
Linnman, C., Moulton, E.A., Barmettler, G., Becerra, L., Borsook, D., 2012. Neuroimaging of the periaqueductal gray: state of the field. Neuroimage 60 (1), 505–522.
Lumb, B.M., 2004. Hypothalamic and midbrain circuitry that distinguishes between escapable and inescapable pain. News Physiol. Sci. 19, 22–26.
Lumb, B.M., Parry, D.M., Semenenko, F.M., McMullan, S., Simpson, D.A., 2002. C-nociceptor activation of hypothalamic neurones and the columnar organisation of their projections to the periaqueductal grey in the rat. Exp. Physiol. 87 (2), 123–128.

Mobbs, D., Petrovic, P., Marchant, J.L., Hassabis, D., Weiskopf, N., Seymour, B., Dolan, R.J., Frith, C.D., 2007. When fear is near: threat imminence elicits prefrontal-periaqueductal gray shifts in humans. Science 317 (5841), 1079–1083.
Mochny, C.R., Kincheski, G.C., Molina, V.A., Carobrez, A.P., 2013. Dorsolateral periaqueductal gray stimulation prior to retrieval potentiates a contextual fear memory in rats. Behav. Brain Res. 237, 76–81.
Napadow, V., Sclocco, R., Henderson, L.A., 2019. Brainstem neuroimaging of nociception and pain circuitries. Pain Rep. 4 (4), e745.
Parry, D.M., Macmillan, F.M., Koutsikou, S., McMullan, S., Lumb, B.M., 2008. Separation of A- versus C-nociceptive inputs into spinal-brainstem circuits. Neuroscience 152 (4), 1076–1085.
Peyron, R., 2014. [Functional imaging of pain]. Biol. Aujourdhui. 208 (1), 5–12.
Preibisch, C., Castrillon, G.J., Buhrer, M., Riedl, V., 2015. Evaluation of Multiband EPI Acquisitions for Resting State fMRI. PLoS ONE 10 (9), e0136961.
Preuschoff, K., Quartz, S.R., Bossaerts, P., 2008. Human insula activation reflects risk prediction errors as well as risk. J. Neurosci. 28 (11), 2745–2752.
Qin, J., Chen, S.G., Hu, D., Zeng, L.L., Fan, Y.M., Chen, X.P., Shen, H., 2015. Predicting individual brain maturity using dynamic functional connectivity. Front. Hum. Neurosci. 9, 418.
Radua, J., Sarro, S., Vigo, T., Alonso-Lana, S., Bonnin, C.M., Ortiz-Gil, J., Canales-Rodriguez, E.J., Maristany, T., Vieta, E., McKenna, P.J., et al., 2014. Common and specific brain responses to scenic emotional stimuli. Brain Struct. Funct. 219 (4), 1463–1472.
Roelofs, K., 2017. Freeze for action: neurobiological mechanisms in animal and human freezing. Philos. Trans. R. Soc. Lond. B Biol. Sci. (1718) 372.
Roy, M., Shohamy, D., Daw, N., Jepma, M., Wimmer, G.E., Wager, T.D., 2014. Representation of aversive prediction errors in the human periaqueductal gray. Nat. Neurosci. 17 (11), 1607–1612.
Rubinov, M., Sporns, O., 2010. Complex network measures of brain connectivity: uses and interpretations. Neuroimage 52 (3), 1059–1069.
Saghayi, M., Greenberg, J., O'Grady, C., Varno, F., Hashmi, M.A., Bracken, B., Matwin, S., Lazar, S.W., Hashmi, J.A., 2020. Brain network topology predicts participant adherence to mental training programs. Netw. Neurosci. 4 (3), 528–555.
Samineni, V.K., Premkumar, L.S., Faingold, C.L., 2017. Neuropathic pain-induced enhancement of spontaneous and pain-evoked neuronal activity in the periaqueductal gray that is attenuated by gabapentin. Pain 158 (7), 1241–1253.
Satpute, A.B., Wager, T.D., Cohen-Adad, J., Bianciardi, M., Choi, J.K., Buhle, J.T., Wald, L.L., Barrett, L.F., 2013. Identification of discrete functional subregions of the human periaqueductal gray. Proc. Natl. Acad. Sci. U. S. A. 110 (42), 17101–17106.
Scott, D.J., Stohler, C.S., Egnatuk, C.M., Wang, H., Koeppe, R.A., Zubieta, J.K., 2008. Placebo and nocebo effects are defined by opposite opioid and dopaminergic responses. Arch. Gen. Psychiatry 65 (2), 220–231.
Seymour, B., 2019. Pain: a Precision Signal for Reinforcement Learning and Control. Neuron 101 (6), 1029–1041.
Seymour, B., Mancini, F., 2020. Hierarchical models of pain: inference, information-seeking, and adaptive control. Neuroimage 222, 117212.
Suarez, L.E., Markello, R.D., Betzel, R.F., Misic, B., 2020. Linking structure and function in macroscale brain networks. Trends Cogn. Sci. 24 (4), 302–315.
Tinnermann, A., Geuter, S., Sprenger, C., Finsterbusch, J., Buchel, C., 2017. Interactions between brain and spinal cord mediate value effects in nocebo hyperalgesia. Science 358 (6359), 105–108.
Tovote, P., Esposito, M.S., Botta, P., Chaudun, F., Fadok, J.P., Markovic, M., Wolff, S.B., Ramakrishnan, C., Fenno, L., Deisseroth, K., et al., 2016. Midbrain circuits for defensive behaviour. Nature 534 (7606), 206–212.
Upadhyay, J., Maleki, N., Potter, J., Elman, I., Rudrauf, D., Knudsen, J., Wallin, D., Pendse, G., McDonald, L., Griffin, M., et al., 2010. Alterations in brain structure and functional connectivity in prescription opioid-dependent patients. Brain 133 (Pt 7), 2098–2114.
Wager, T.D., Atlas, L.Y., Lindquist, M.A., Roy, M., Woo, C.W., Kross, E., 2013. An fMRI-based neurologic signature of physical pain. N. Engl. J. Med. 368 (15), 1388–1397.
Walker, P., Carrive, P., 2003. Role of ventrolateral periaqueductal gray neurons in the behavioral and cardiovascular responses to contextual conditioned fear and poststress recovery. Neuroscience 116 (3), 897–912.
Watson, T.C., Cerminara, N.L., Lumb, B.M., Apps, R., 2016. Neural correlates of fear in the periaqueductal gray. J. Neurosci. 36 (50), 12707–12719.
Woolrich, M.W., Jbabdi, S., Patenaude, B., Chappell, M., Makni, S., Behrens, T., Beckmann, C., Jenkinson, M., Smith, S.M., 2009. Bayesian analysis of neuroimaging data in FSL. Neuroimage 45 (1), S173–S186 Suppl.
Wright, K.M., Jhou, T.C., Pimpinelli, D., McDannald, M.A., 2019. Cue-inhibited ventrolateral periaqueductal gray neurons signal fear output and threat probability in male rats. Elife 8.
Wright, K.M., McDannald, M.A., 2019. Ventrolateral periaqueductal gray neurons prioritize threat probability over fear output. Elife 8.
Young, C.B., Raz, G., Everaerd, D., Beckmann, C.F., Tendolkar, I., Hendler, T., Fernandez, G., Hermans, E.J., 2017. Dynamic Shifts in Large-Scale Brain Network Balance As a Function of Arousal. J. Neurosci. 37 (2), 281–290.